

Isogeometric continuity constraints for multi-patch shells governed by fourth-order deformation and phase field models

Karsten Paul*, Christopher Zimmermann*, Thang X. Duong*, Roger A. Sauer*,^{†1}

**Aachen Institute for Advanced Study in Computational Engineering Science (AICES),
RWTH Aachen University, Templergraben 55, 52062 Aachen, Germany*

[†]Department of Mechanical Engineering, Indian Institute of Technology Kanpur, UP 208016, India

Abstract

This work presents numerical techniques to enforce continuity constraints on multi-patch surfaces for three distinct problem classes. The first involves structural analysis of thin shells that are described by general Kirchhoff-Love kinematics. Their governing equation is a vector-valued, fourth-order, nonlinear, partial differential equation (PDE) that requires at least C^1 -continuity within a displacement-based finite element formulation. The second class are surface phase separations modeled by a phase field. Their governing equation is the Cahn-Hilliard equation a scalar, fourth-order, nonlinear PDE that can be coupled to the thin shell PDE. The third class are brittle fracture processes modeled by a phase field approach. In this work, these are described by a scalar, fourth-order, nonlinear PDE that is similar to the Cahn-Hilliard equation and is also coupled to the thin shell PDE. Using a direct finite element discretization, the two phase field equations also require at least a C^1 -continuous formulation. Isogeometric surface discretizations often composed of multiple patches thus require constraints that enforce the C^1 -continuity of displacement and phase field. For this, two numerical strategies are presented: A Lagrange multiplier formulation and a penalty regularization. They are both implemented within the curvilinear shell and phase field formulations of [Duong et al. \(2017\)](#), [Zimmermann et al. \(2019\)](#) and [Paul et al. \(2019\)](#) and illustrated by several numerical examples. These consider deforming shells, phase separations on evolving surfaces, and dynamic brittle fracture.

Keywords: Isogeometric analysis, Kirchhoff-Love shells, phase field methods, Cahn-Hilliard equation, brittle fracture, higher-order PDEs

1 Introduction

Thin-walled structures commonly appear in engineering design since they combine the advantages of low weight and high strength. Kirchhoff-Love (KL) theory is a suitable choice to model these, especially if the slenderness ratio is high. This theory contains higher order derivatives, so that the geometric discretization requires higher continuity than that of standard finite elements. Likewise, diffusion problems are also often described with higher order operators, which necessitates a higher continuous approximation space for the test and trial functions. The same holds true for higher-order fracture models. Isogeometric analysis (IGA) offers the possibility of user-defined smoothness in the geometry and solution. IGA works simplest on a single patch of elements that is discretized with Non-Uniform Rational B-Splines (NURBS). But in real-world problems, single patches are often not sufficient to represent arbitrarily complex shapes

¹corresponding author, email: sauer@aices.rwth-aachen.de

or topologies. Instead, multi-patch descriptions are used to describe these geometries, but the higher continuity is not automatically preserved across the patch interfaces. This work presents a general framework to model coupled problems, in which diffusion and fracture processes take place on deforming thin shells, using multi-patch NURBS discretizations and corresponding patch constraints. The latter enforce the continuity of the surface normal and phase field gradient in order to accurately transfer stresses, moments and mass fluxes at patch interfaces.

Several models have been proposed to describe isogeometric KL shells, starting with [Kiendl et al. \(2009\)](#). KL shell theory only uses displacement degrees-of-freedom (dofs), which distinguishes it from thick shell theories, such as the Reissner-Mindlin shell theory. The pure displacement formulation results in a partial differential equation (PDE) that contains fourth-order derivatives. The required high continuity is obtained by means of isogeometric shape functions. At least C^1 -continuity is required in a Galerkin-type finite element formulation.

The current work studies two coupled models representing two different physical processes on deforming thin shells. Their resulting finite element formulation shows many similarities. The first model is a phase field formulation for phase separations based on the Cahn-Hilliard theory ([Cahn and Hilliard, 1958](#); [Cahn, 1961](#)). The theory of coupling in-plane phase transitions and surface deformations is taken from [Sahu et al. \(2017\)](#). The second model investigates brittle fracture based on an adaptive phase field framework. Here, the stored elastic energy drives crack evolution and material parameters are degraded in regions of fracture. As for the Cahn-Hilliard theory, this model resembles a diffuse interface model in which the transition zone between different phases is smeared out. The foundation for brittle fracture has been established by [Griffith \(1921\)](#), reformulated by [Francfort and Marigo \(1998\)](#) and first implemented within a finite element method by [Bourdin et al. \(2000\)](#). The structural shell formulation for both models is taken from the work of [Duong et al. \(2017\)](#) and the individual coupling is described in detail in [Zimmermann et al. \(2019\)](#) and [Paul et al. \(2019\)](#). Both models lead to a coupled formulation of two nonlinear fourth-order PDEs that are defined on an evolving two-dimensional manifold.

In IGA, introduced by [Hughes et al. \(2005\)](#), splines are used to describe the geometry and the approximate solution. This offers the possibility of discretizations with high continuity. The local spatial refinement of these, which may be necessary to obtain a highly resolved mesh at phase interfaces, has been studied in several works: [Forsey and Bartels \(1988\)](#) introduce hierarchical B-splines. In the work of [Sederberg et al. \(2003\)](#) and [Scott et al. \(2012\)](#), T-splines are investigated for local refinement. Locally Refinable (LR) B-splines are introduced by [Dokken et al. \(2013\)](#) and advanced by [Johannessen et al. \(2014\)](#). An extension to LR NURBS is given by [Zimmermann and Sauer \(2017\)](#). Recently, the combination of T- and LR-splines is proposed by the introduction of LR T-splines in [Chen and de Borst \(2018\)](#). Additionally, unstructured spline spaces are introduced to represent more complex geometries in an IGA-suitable manner, for instance in [Toshniwal et al. \(2017\)](#).

In Tab. 1, existing techniques for patch coupling in isogeometric analysis are illustrated. They are needed to transfer quantities across patch interfaces, such as stresses, moments and mass fluxes. For each method, the main properties and references to publications are given.

Table 1: Existing techniques for patch coupling in isogeometric analysis.

Name	Properties	Publications
Penalty method	<ul style="list-style-type: none"> + No additional dofs + Easy implementation + Non-conforming meshes – Possible ill-conditioning – Variational inconsistency 	Apostolatos et al. (2014) ; Lei et al. (2015) ; Duong et al. (2017) ; Apostolatos et al. (2019) ; Horger et al. (2019) ; Herrema et al. (2019)
Lagrange multiplier method	<ul style="list-style-type: none"> + Constraint exactly fulfilled – Additional dofs – Need to ensure LBB stability 	Apostolatos et al. (2014) ; Duong et al. (2017) ; Sommerwerk et al. (2017) ; Apostolatos et al. (2019)
Bending strip method	<ul style="list-style-type: none"> + Easy implementation – Possible ill-conditioning – Only conforming meshes 	Kiendl et al. (2010) ; Goyal and Simeon (2017)
Mortar method (based on Lagrange multipliers)	<ul style="list-style-type: none"> + Non-conforming meshes + Increased robustness due to averaging quantities on slave-body – Additional dofs 	Dornisch et al. (2015) ; Bouclier et al. (2017) ; Hirschler et al. (2019) ; Horger et al. (2019) ; Schu et al. (2019)
Nitsche’s method	<ul style="list-style-type: none"> + Non-conforming meshes + Variational consistency + Stiffness matrix well conditioned and semi-positive-definite + No additional dofs – A formulation for general problems is difficult and complex 	Nguyen et al. (2014) ; Apostolatos et al. (2014) ; Ruess et al. (2014) ; Du et al. (2015) ; Guo and Ruess (2015) ; Bouclier et al. (2017) ; Gu et al. (2018) ; Hu et al. (2018) ; Apostolatos et al. (2019)
Direct elimination of constraints	<ul style="list-style-type: none"> + Less dofs + Stiffness matrix dimension reduces – Only conforming meshes – Large implementation effort 	Lei et al. (2015) ; Coox et al. (2017) ; Duong et al. (2017)

There are also other works that cannot be categorized as above. [Kiendl et al. \(2009\)](#) construct G^1 -continuous KL shell parametrizations by coupling the first and second rows of control points at patch interfaces with each other. This method is restricted to conforming meshes and smooth interfaces. T-splines are further examined on non-conforming two-patch geometries by [Beirão da Veiga et al. \(2011\)](#). [Collin et al. \(2016\)](#) study h -refinement and introduce analysis suitable G^1 -geometry parametrizations on multi-patches. In [Chan et al. \(2018\)](#), linear elasticity, KL shells and the Cahn-Hilliard equation are studied. They propose a method to overcome C^1 -locking by local degree elevation along patch interfaces. C^1 -locking refers to restricted convergence rates due to overconstraining of the solution space ([Collin et al., 2016](#)). [Schu et al. \(2019\)](#) consider higher-order Dirichlet boundary conditions and higher-order patch coupling conditions in KL shell elements. They propose a least-squares approach to incorporate constraints into the IGA approximation space and they compare their results to a mortar approach.

The present work extends the general geometrical constraint formulation of [Duong et al. \(2017\)](#) to coupled problems describing Cahn-Hilliard-type phase transitions on deforming thin shells ([Zimmermann et al., 2019](#)), and a phase field based fracture of brittle shells ([Paul et al., 2019](#)). Patch constraints that enforce the required C^1 -continuity of the phase field across patch interfaces are presented, and their accuracy and convergence behavior is studied. Summarizing, the proposed formulation includes following highlights:

- It uses constraints to enforce G^1 -continuity on multi-patch NURBS.
- It is fully formulated in a curvilinear coordinate system.
- It proposes a new constraint for C^1 -continuous phase fields on multi-patch NURBS.
- It exhibits excellent accuracy compared to single patch discretizations.
- It is capable to describe fracture branching across kinked surfaces.
- The proposed constraints are validated by several nonlinear benchmark problems.

The remainder of this paper is structured as follows: Sec. 2 summarizes the employed thin shell framework. The computational formulation for the Cahn-Hilliard phase separation model is summarized in Sec. 3. In Sec. 4, the computational phase field model of brittle shells is outlined. The proposed formulation for the required patch constraints is discussed in Sec. 5. Numerical examples that highlight the effect of these constraints on the numerical solution are shown in Sec. 6. This paper concludes with a summary and an outlook in Sec. 7.

2 Thin shell theory

This paper deals with thin shell theory and their coupling to two phase field models, see Fig. 1. This section summarizes the computational description of thin shells, while binary mixtures and fracture follow in Secs 3–4. At first, a short introduction to the surface description is given,

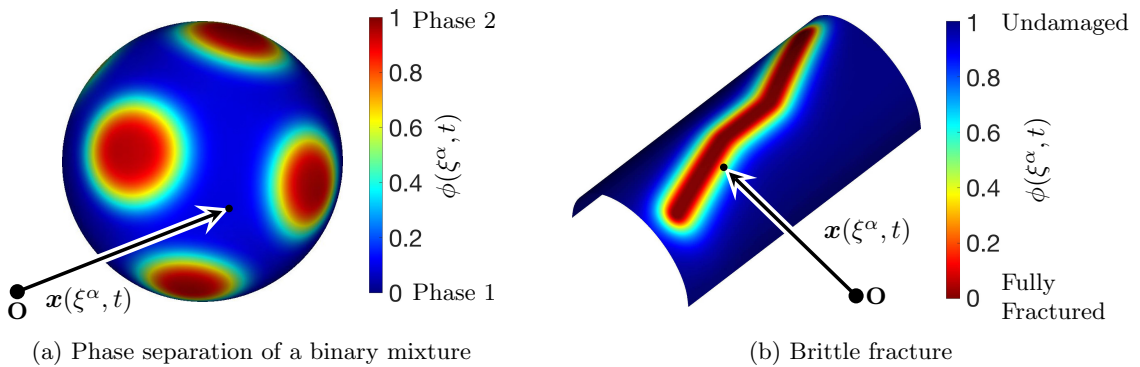


Figure 1: Two cases of phase fields on curved shells. (a) Phase separation of a binary mixture, where ϕ describes the mixture of two phases, and (b) fracture, where ϕ distinguishes between undamaged and fully fractured material.

which is then followed by the discretized weak form and constitutive relations. A mathematical background as well as a much more detailed description can be found for example in [Sauer \(2018\)](#).

2.1 Surface description

Following the framework of differential geometry, a curved surface \mathcal{S} is described by a convected coordinate system and the mapping

$$\mathbf{x} = \mathbf{x}(\xi^\alpha, t), \quad (1)$$

between the parameter domain and the physical surface. Here, ξ^α , $\alpha = 1, 2$, denote the convective coordinates and t denotes time.² The phase field is denoted $\phi(\xi^\alpha, t)$ and ranges from 0 to 1, see Fig. 1. The mapping in Eq. (1) then defines a set of surface points $\mathbf{x} \in \mathcal{S}$ to represent the surface. A co-variant basis $\{\mathbf{a}_\alpha, \mathbf{n}\}$ is associated with each of these surface points with co-variant tangent vectors \mathbf{a}_α and surface normal \mathbf{n} defined by

$$\mathbf{a}_\alpha := \frac{\partial \mathbf{x}}{\partial \xi^\alpha}, \quad \mathbf{n} := \frac{\mathbf{a}_1 \times \mathbf{a}_2}{\|\mathbf{a}_1 \times \mathbf{a}_2\|}. \quad (2)$$

The co-variant surface metric with components

$$a_{\alpha\beta} := \mathbf{a}_\alpha \cdot \mathbf{a}_\beta, \quad (3)$$

then follows. Orthonormality in the basis is achieved by the introduction of a contra-variant basis $\{\mathbf{a}^\alpha, \mathbf{n}\}$, such that $\mathbf{a}_\alpha \cdot \mathbf{a}^\beta = \delta_\alpha^\beta$, with Kronecker delta δ_α^β . The contra-variant tangent vectors are given by

$$\mathbf{a}^\alpha = a^{\alpha\beta} \mathbf{a}_\beta, \quad (4)$$

where the contra-variant surface metric $a^{\alpha\beta}$ follows from the inverse of the co-variant surface metric, i.e. $[a^{\alpha\beta}] = [a_{\alpha\beta}]^{-1}$. The second parametric derivative $\mathbf{a}_{\alpha,\beta} := \partial \mathbf{a}_\alpha / \partial \xi^\beta$ is introduced in order to determine the curvature components and the mean curvature, i.e.

$$b_{\alpha\beta} := \mathbf{a}_{\alpha,\beta} \cdot \mathbf{n}, \quad H := a^{\alpha\beta} b_{\alpha\beta} / 2. \quad (5)$$

Based on this geometric representation of surface \mathcal{S} , surface operators can be defined, namely the surface gradient and surface Laplacian of a general scalar ϕ , and the surface divergence of a general vector \mathbf{v} ,

$$\begin{aligned} \text{grad}_s \phi &:= \nabla_s \phi &:= \phi_{;\alpha} \mathbf{a}^\alpha, \\ \text{div}_s \mathbf{v} &:= \nabla_s \cdot \mathbf{v} &:= \mathbf{v}_{;\alpha} \cdot \mathbf{a}^\alpha, \\ \Delta_s \phi &:= \nabla_s \cdot \nabla_s \phi &= \phi_{;\alpha\beta} a^{\alpha\beta}. \end{aligned} \quad (6)$$

The subscript ‘;’ is used to describe the co-variant derivative, given as

$$\begin{aligned} \phi_{;\alpha} &= \phi_{,\alpha}, \\ \mathbf{v}_{;\alpha} &= \mathbf{v}_{,\alpha}, \\ \phi_{;\alpha\beta} &= \phi_{,\alpha\beta} - \Gamma_{\alpha\beta}^\gamma \phi_{,\gamma}, \end{aligned} \quad (7)$$

with $\dots_{,\alpha} := \partial \dots / \partial \xi^\alpha$ and the Christoffel symbols of the second kind $\Gamma_{\alpha\beta}^\gamma := \mathbf{a}_{\alpha,\beta} \cdot \mathbf{a}^\gamma$ on \mathcal{S} .

2.2 Discretization of primary fields

Subsequently, the finite element (FE) approximations of the primary fields, the deformation and phase field, are outlined. The n_e spline basis functions on element Ω^e are numbered with

²All Greek indices run from 1 to 2 and obey Einstein’s summation convention.

global indices i_1, \dots, i_{n_e} . The FE approximations of \mathbf{x} and its variation $\delta\mathbf{x}$ can then be written as

$$\mathbf{x} \approx \mathbf{N} \mathbf{x}_e, \quad \text{and} \quad \delta\mathbf{x} \approx \mathbf{N} \delta\mathbf{x}_e, \quad (8)$$

with \mathbf{x}_e and $\delta\mathbf{x}_e$ describing the element-level vectors of nodal values and their variation. Further, the corresponding shape function array is given by

$$\mathbf{N} = [N_{i_1} \mathbf{1}, N_{i_2} \mathbf{1}, \dots, N_{i_{n_e}} \mathbf{1}], \quad (9)$$

with $\mathbf{1}$ denoting the (3×3) -identity matrix. The FE approximations of the phase field ϕ and its variation $\delta\phi$ follow in analogy, i.e.

$$\phi \approx \bar{\mathbf{N}} \phi_e, \quad \text{and} \quad \delta\phi \approx \bar{\mathbf{N}} \delta\phi_e, \quad (10)$$

with shape function array

$$\bar{\mathbf{N}} := [N_{i_1}, N_{i_2}, \dots, N_{i_{n_e}}]. \quad (11)$$

The element-level vectors of nodal phase values and variations are denoted ϕ_e and $\delta\phi_e$, respectively.

2.3 Discretized mechanical weak form

The discretized mechanical weak form can be written as (Duong et al., 2017)

$$\delta\mathbf{x}^T [\mathbf{f}_{\text{in}} + \mathbf{f}_{\text{int}} - \mathbf{f}_{\text{ext}}] = 0, \quad \forall \delta\mathbf{x} \in \mathcal{U}^h, \quad (12)$$

where the global force vectors \mathbf{f}_{in} , \mathbf{f}_{int} and \mathbf{f}_{ext} are assembled from their respective elemental contributions

$$\begin{aligned} \mathbf{f}_{\text{in}}^e &:= \mathbf{m}_e \ddot{\mathbf{x}}_e, \quad \mathbf{m}_e := \int_{\Omega^e} \rho(\phi) \mathbf{N}^T \mathbf{N} \, da, \\ \mathbf{f}_{\text{int}}^e &:= \int_{\Omega^e} \sigma^{\alpha\beta}(\phi) \mathbf{N}_{,\alpha}^T \mathbf{a}_\beta \, da + \int_{\Omega^e} M^{\alpha\beta}(\phi) \mathbf{N}_{;\alpha\beta}^T \mathbf{n} \, da, \\ \mathbf{f}_{\text{ext}}^e &:= \int_{\Omega^e} \mathbf{N}^T p(\phi) \mathbf{n} \, da + \int_{\Omega^e} \mathbf{N}^T f^\alpha(\phi) \mathbf{a}_\alpha \, da, \end{aligned} \quad (13)$$

with shape function array from Eq. (9). Further, \mathcal{U}^h resembles the respective discrete space, and $\mathbf{N}_{;\alpha\beta}^T$ follows in analogy to Eq. (7.3). The density is $\rho(\phi)$, the prescribed body forces are $\mathbf{f}(\phi) = f^\alpha(\phi) \mathbf{a}_\alpha + p(\phi) \mathbf{n}$, and the stress and moment components are $\sigma^{\alpha\beta}(\phi)$ and $M^{\alpha\beta}(\phi)$, respectively. Note that boundary loads acting on $\partial\mathcal{S}$ are assumed to be zero in the above expression of $\mathbf{f}_{\text{ext}}^e$. The corresponding extension to boundary loads is described in Duong et al. (2017). From Eq. (12) follows the equation of motion of the free nodes (where no Dirichlet boundary conditions are prescribed)

$$\mathbf{f}(\mathbf{x}, \phi) = \mathbf{M} \ddot{\mathbf{x}} + \mathbf{f}_{\text{int}}(\mathbf{x}, \phi) - \mathbf{f}_{\text{ext}}(\mathbf{x}, \phi) = \mathbf{0}, \quad (14)$$

where \mathbf{x} and ϕ are the global unknowns corresponding to \mathbf{x}_e and ϕ_e . The global mass matrix \mathbf{M} follows from the assembly of the matrices \mathbf{m}_e . Eq. (14) can be solved by itself in case ϕ is not an unknown, as in the examples of Sec. 6.1.

2.4 Constitutive relations

The constitutive behavior follows from the Helmholtz free energy function

$$\Psi = \Psi_{\text{el}} + \Psi_{\text{phase}}. \quad (15)$$

The second term is discussed in Secs. 3.2 and 4.2. For the first term, a hyperelastic material behavior with an elastic energy density $\Psi_{\text{el}} = \Psi_{\text{el}}(a_{\alpha\beta}, b_{\alpha\beta}, \phi)$ is assumed. It is determined from membrane and bending contributions. The first is given by a Neo-Hookean material model (Sauer and Duong, 2017)

$$\Psi_{\text{dil}} = \frac{K}{4}(J^2 - 1 - 2 \ln J), \quad \text{and} \quad \Psi_{\text{dev}} = \frac{G}{2}(I_1/J - 2), \quad (16)$$

and the second one by a part of the Koiter model (Ciarlet, 1993)

$$\Psi_{\text{bend}} = \frac{c}{2}(b_{\alpha\beta} - B_{\alpha\beta})(b_0^{\alpha\beta} - B^{\alpha\beta}), \quad b_0^{\alpha\beta} := A^{\alpha\gamma}b_{\gamma\delta}A^{\beta\delta}. \quad (17)$$

The two invariants in Eq. (16) read

$$I_1 := A^{\alpha\beta}a_{\alpha\beta} \quad \text{and} \quad J := \sqrt{\det[A^{\alpha\beta}] \det[a_{\alpha\beta}]}, \quad (18)$$

with contra-variant metric $A^{\alpha\beta}$ in the reference configuration. The 2D bulk, 2D shear, and bending moduli are denoted K , G , and c , respectively, and they are generally a function of the phase variable ϕ . The stress and moment components follow from

$$\begin{aligned} \sigma^{\alpha\beta} &= \frac{2}{J} \frac{\partial \Psi}{\partial a_{\alpha\beta}} - \eta \dot{a}^{\alpha\beta}, \\ M^{\alpha\beta} &= \frac{1}{J} \frac{\partial \Psi}{\partial b_{\alpha\beta}}. \end{aligned} \quad (19)$$

Eq. (19.1) represents a Kelvin model to account for viscous in-plane stresses. In this model, a spring and dashpot act in parallel and thus, their stresses are added.³ The dynamic surface viscosity is denoted η . More complex constitutive models require a general strain decomposition, which has been recently formulated for Kirchhoff-Love shells in Sauer et al. (2019). For the given material model, the individual contributions to the stress components are given by

$$\begin{aligned} \sigma_{\text{dil}}^{\alpha\beta} &= \frac{K}{2J}(J^2 - 1)a^{\alpha\beta}, \\ \sigma_{\text{dev}}^{\alpha\beta} &= \frac{G}{2J^2}(2A^{\alpha\beta} - I_1 a^{\alpha\beta}), \\ \sigma_{\text{visc}}^{\alpha\beta} &= -\eta \dot{a}^{\alpha\beta}. \end{aligned} \quad (20)$$

Likewise, the moment components stemming from Eq. (17) are

$$M^{\alpha\beta} = \frac{c}{J}(b_0^{\alpha\beta} - B^{\alpha\beta}). \quad (21)$$

Note that Eqs. (20)–(21) do not contain the stresses and moments coming from the phase field model. These are further described in Secs. 3.2 and 4.2.

³In Eq. (19), $\dot{a}^{\alpha\beta} = -a^{\alpha\gamma} \dot{a}_{\gamma\delta} a^{\delta\beta}$ are the components of the symmetric surface velocity gradient, e.g. see Sauer (2018).

3 Phase transitions on deforming surfaces

This section briefly summarizes the discretized weak form and constitutive relations describing phase transitions on deforming surfaces according to the computational model of [Zimmermann et al. \(2019\)](#). In the following, the dimensionless concentration field $\phi(\xi^\alpha, t)$ is used to describe the local density fractions of binary mixtures, see Fig. 1a.⁴

3.1 Discretized weak form

The discretized weak form of the surface Cahn-Hilliard equation can be written as

$$\delta\phi^T [\bar{\mathbf{f}}_{\text{in}} + \bar{\mathbf{f}}_{\text{int}} - \bar{\mathbf{f}}_{\text{ext}}] = 0, \quad \forall \delta\phi \in \mathcal{V}^h. \quad (22)$$

The global vectors $\bar{\mathbf{f}}_{\text{in}}$, $\bar{\mathbf{f}}_{\text{int}}$ and $\bar{\mathbf{f}}_{\text{ext}}$ are assembled from their respective elemental contributions

$$\begin{aligned} \bar{\mathbf{f}}_{\text{in}}^e &:= \bar{\mathbf{m}}_e \dot{\phi}_e, \quad \bar{\mathbf{m}}_e := \int_{\Omega^e} \rho \bar{\mathbf{N}}^T \bar{\mathbf{N}} \, da, \\ \bar{\mathbf{f}}_{\text{int}}^e &:= \bar{\mathbf{k}}_e \phi_e - \bar{\mathbf{f}}_{\text{el}}^e, \quad \bar{\mathbf{k}}_e := \int_{\Omega_0^e} \left[\bar{\mathbf{N}}_{,\alpha}^T a^{\alpha\beta} \left(M \mu'_\phi - M'(\mu_i + \mu_{\text{el}}) \right) \bar{\mathbf{N}}_{,\beta} + \Delta_s \bar{\mathbf{N}}^T J \ell^2 M \Delta_s \bar{\mathbf{N}} \right] dA, \\ \bar{\mathbf{f}}_{\text{el}}^e &:= \int_{\Omega_0^e} \Delta_s \bar{\mathbf{N}}^T M \mu_{\text{el}} \, dA, \\ \bar{\mathbf{f}}_{\text{ext}}^e &:= \mathbf{0}. \end{aligned} \quad (23)$$

Further, \mathcal{V}^h represents the respective discrete space, and $\Delta_s \bar{\mathbf{N}}$ follows in analogy to Eq. (6.3). Further, $M = D\phi(1-\phi)$, $D = \text{const}$, denotes the degenerate mobility, ℓ represents the length scale of the phase interface and J is the surface stretch, see Eq. (18.2). The remaining terms in Eq. (23) are described in Sec. 3.2. Note that boundary loads are assumed to be zero in the above expression of $\bar{\mathbf{f}}_{\text{ext}}^e$. The corresponding extension to boundary loads is described in [Zimmermann et al. \(2019\)](#). From Eq. (22) follows the evolution equation for ϕ at the free nodes (after application of Dirichlet boundary conditions)

$$\bar{\mathbf{f}}(\mathbf{x}, \phi) = \bar{\mathbf{M}} \dot{\phi} + \bar{\mathbf{f}}_{\text{int}}(\mathbf{x}, \phi) - \bar{\mathbf{f}}_{\text{ext}}(\mathbf{x}) = \mathbf{0}, \quad (24)$$

with global mass matrix $\bar{\mathbf{M}}$ being assembled from $\bar{\mathbf{m}}_e$. Together, Eqs. (14) and (24) describe a coupled chemo-mechanical problem. It is discretized and integrated in time with an implicit, monolithic and adaptive method ([Zimmermann et al., 2019](#)) based on the generalized- α scheme by [Chung and Hulbert \(1993\)](#).

3.2 Constitutive relations

The material parameters are assumed to depend on the concentration field ϕ via the following mixture rules

$$\begin{aligned} K(\phi) &= K_1 f(\phi) + K_0 (1 - f(\phi)), \quad G(\phi) = G_1 f(\phi) + G_0 (1 - f(\phi)), \\ c(\phi) &= c_1 f(\phi) + c_0 (1 - f(\phi)), \quad \eta(\phi) = \eta_1 f(\phi) + \eta_0 (1 - f(\phi)), \end{aligned} \quad (25)$$

with the interpolation function

$$f(\phi) = \frac{1}{2} \left(1 + \tanh(-\rho_{\text{sh}} \pi + 4 \pi \phi) \right). \quad (26)$$

⁴The concentration field ϕ is also referred to as the *order parameter field* or *phase field* in the literature.

Here, K_i , G_i , c_i and η_i ($i = 0, 1$) are the material parameters of the two components. The parameter $\rho_{\text{sh}} \in \mathbb{R}$ specifies whether a small or a large portion of the phase interface is characterized by material properties at $\phi = 1$. The force vectors in Eq. (23) include the chemical potential μ that has the contributions μ_{b} , μ_{i} , μ_{el} , μ_{ϕ} associated with the bulk, interface, elastic, and mixing energy, given by

$$\begin{aligned}\mu_{\text{b}} &= \mu_{\phi} + \mu_{\text{el}}, & \mu_{\phi} &= N k_{\text{B}} T \ln \frac{\phi}{1-\phi} + N \omega (1-2\phi), \\ \mu_{\text{el}} &= \Psi'_{\text{el}}, & \mu_{\text{i}} &= -J N \omega \ell^2 \Delta_{\text{s}} \phi,\end{aligned}\tag{27}$$

where $(\dots)' := \partial \dots / \partial \phi$. Further, N denotes the number of molecules per reference area, k_{B} is Boltzmann's constant and $\omega = 2 k_{\text{B}} T_{\text{c}}$ is a bulk energy that is related to the critical temperature T_{c} at which phase separation occurs.

The Cahn-Hilliard energy in Eq. (15) is given by

$$\Psi_{\text{phase}} = N \omega \phi (1-\phi) + T N k_{\text{B}} (\phi \ln \phi + (1-\phi) \ln (1-\phi)) + J N \omega \frac{\ell^2}{2} \nabla_{\text{s}} \phi \cdot \nabla_{\text{s}} \phi.\tag{28}$$

The stresses stemming from Ψ_{phase} are denoted Korteweg stresses and are given by

$$\sigma_{\text{CH}}^{\alpha\beta} = N \omega \frac{\ell^2}{2} \left(a^{\alpha\beta} a^{\gamma\delta} - 2 a^{\alpha\gamma} a^{\beta\delta} \right) \phi_{;\gamma} \phi_{;\delta}.\tag{29}$$

Note that there are no bending moments induced by the Cahn-Hilliard energy.

4 Brittle fracture of deforming thin shells

This section summarizes the phase field model for brittle fracture of thin shells by [Paul et al. \(2019\)](#). In phase field methods, cracks are smeared out and described by a field $\phi(\xi^{\alpha}, t) \in [0, 1]$, see Fig. 1b.⁵ It indicates fully fractured ($\phi = 0$) and undamaged ($\phi = 1$) material. A length scale parameter ℓ_0 [m] gives control over the support width of the phase field profile, i.e. $\text{supp}(\phi) \sim \ell_0$.

4.1 Discretized weak form

The phase field evolution equation is determined from the minimization of the Helmholtz free energy that consists of elastic and fracture contributions, see Sec. 4.2. Based on this, the discretized weak form of the phase field evolution equation becomes

$$\delta \phi^{\text{T}} [\bar{\mathbf{f}}_{\text{el}} + \bar{\mathbf{f}}_{\text{frac}}] = 0, \quad \forall \delta \phi \in \mathcal{V}^h,\tag{30}$$

with the elemental contributions

$$\begin{aligned}\bar{\mathbf{f}}_{\text{el}}^e &:= \int_{\Omega_0^e} \bar{\mathbf{N}}^{\text{T}} \frac{2\ell_0}{\mathcal{G}_{\text{c}}} g'(\phi) \mathcal{H} \, \text{d}A, \\ \bar{\mathbf{f}}_{\text{frac}}^e &:= \int_{\Omega_0^e} \left[\bar{\mathbf{N}}^{\text{T}} \bar{\mathbf{N}} + \bar{\mathbf{N}}_{,\alpha}^{\text{T}} 2 \ell_0^2 A^{\alpha\beta} \bar{\mathbf{N}}_{,\beta} + \Delta_{\text{S}} \bar{\mathbf{N}}^{\text{T}} \ell_0^4 \Delta_{\text{S}} \bar{\mathbf{N}} \right] \phi_e \, \text{d}A - \int_{\Omega_0^e} \bar{\mathbf{N}}^{\text{T}} \, \text{d}A.\end{aligned}\tag{31}$$

The shape function array for the phase field is denoted $\bar{\mathbf{N}}$, see Eq. (11), and $\Delta_{\text{S}} \bar{\mathbf{N}}$ follows in analogy to Eq. (6.3). Note that here, the surface Laplacian is defined on the reference

⁵The phase field ϕ is also referred to as the *fracture field* in the literature.

configuration. The fracture toughness is denoted \mathcal{G}_c . The degradation function (Borden et al., 2016)

$$g(\phi) = (3 - s)\phi^2 - (2 - s)\phi^3, \quad s = 10^{-4}, \quad (32)$$

controls the loss of material stiffness in regions of fracture and \mathcal{H} is the history field that is motivated and discussed in the next section. The degradation function in Eq. (32) couples the elastic energy density in Eq. (15) with the phase field. The phase field force vector is coupled to the deformation by \mathcal{H} , see Eq. (31.1). The resulting equations at the free nodes simplify to

$$\bar{\mathbf{f}}(\mathbf{x}, \phi) = \bar{\mathbf{f}}_{\text{el}}(\mathbf{x}, \phi) + \bar{\mathbf{f}}_{\text{frac}}(\phi) = \mathbf{0}. \quad (33)$$

To obtain a highly resolved mesh in regions of damage, a local refinement strategy based on LR NURBS is employed (Paul et al., 2019). As for the phase separation process, the temporal discretization is based on the generalized- α scheme by Chung and Hulbert (1993) with an adaptive time-stepping scheme.

4.2 Constitutive relations

Crack evolution shows an anisotropic behavior since it does not occur in compression. Thus, an additive split of the elastic energy density is required,

$$\Psi_{\text{el}} = \Psi_{\text{el}}^+ + \Psi_{\text{el}}^-, \quad (34)$$

that distinguishes between a positive part that contributes to crack evolution, and a negative part, which does not. The elastic part of the Helmholtz free energy in Eq. (15) is thus, changed to

$$\Psi_{\text{el}} = g(\phi) \mathcal{H} + \Psi_{\text{el}}^-, \quad (35)$$

with degradation function $g(\phi)$ from Eq. (32) and the history field $\mathcal{H}(\mathbf{x}, t) = \max_{\tau \in [0, t]} \Psi_{\text{el}}^+(\mathbf{x}, \tau)$ that enforces an irreversible fracture process. The fracture energy is given by (Borden et al., 2014; Paul et al., 2019)

$$\Psi_{\text{phase}} = \frac{\mathcal{G}_c}{4\ell_0} \left[(\phi - 1)^2 + 2\ell_0^2 \nabla_S \phi \cdot \nabla_S \phi + \ell_0^4 (\Delta_S \phi)^2 \right]. \quad (36)$$

The membrane and bending contributions of Ψ_{el} are split separately and the split of Amor et al. (2009) is adopted for the membrane part, i.e.

$$\Psi_{\text{mem}}^+ = \begin{cases} \Psi_{\text{dev}} + \Psi_{\text{dil}}, & J \geq 1 \\ \Psi_{\text{dev}}, & J < 1 \end{cases}, \quad \Psi_{\text{mem}}^- = \begin{cases} 0, & J \geq 1 \\ \Psi_{\text{dil}}, & J < 1 \end{cases}, \quad (37)$$

with dilatational and deviatoric energies taken from Eq. (16) and surface stretch J from Eq. (18.2). Now, the total stresses in the system are

$$\sigma^{\alpha\beta} = g(\phi) \sigma_+^{\alpha\beta} + \sigma_-^{\alpha\beta}, \quad (38)$$

with

$$\sigma_+^{\alpha\beta} = \begin{cases} \sigma_{\text{dev}}^{\alpha\beta} + \sigma_{\text{dil}}^{\alpha\beta}, & J \geq 1 \\ \sigma_{\text{dev}}^{\alpha\beta}, & J < 1 \end{cases}, \quad \text{and} \quad \sigma_-^{\alpha\beta} = \begin{cases} 0, & J \geq 1 \\ \sigma_{\text{dil}}^{\alpha\beta}, & J < 1 \end{cases}, \quad (39)$$

and contributions from Eqs. (20.1)–(20.2). The degradation function $g(\phi)$ is given in Eq. (32). The brittle fracture model does not incorporate viscosity, such that $\eta = 0$, see Eq. (19.1).

The bending part of the elastic energy density is split based on thickness integration (Paul et al., 2019). According to this, the bending energy density Ψ_{bend} is constructed from the three-dimensional Saint Venant-Kirchhoff model (Duong et al., 2017)

$$\Psi_{\text{bend},3\text{D}}(\mathbf{K}, \xi, T) = \xi^2 \frac{12}{T^3} \frac{c}{2} \text{tr}(\mathbf{K}^2), \quad (40)$$

with the relative symmetric curvature tensor $\mathbf{K} = (b_{\alpha\beta} - B_{\alpha\beta})\mathbf{A}^\alpha \otimes \mathbf{A}^\beta$. The energy split is then performed on this three-dimensional constitutive law. Afterwards, it is integrated over the thickness to obtain the energy split in surface energy form, i.e.

$$\Psi_{\text{bend}}^\pm = \int_{-\frac{T}{2}}^{\frac{T}{2}} \Psi_{\text{bend},3\text{D}}^\pm(\xi) d\xi. \quad (41)$$

In analogy to Eq. (37), the split of Eq. (40) is based on the surface stretch \tilde{J} at the shell layer at position $\xi \in [-T/2, T/2]$, i.e.

$$\Psi_{\text{bend},3\text{D}}^+(\xi) = \begin{cases} \xi^2 \frac{12}{T^3} \frac{c}{2} \text{tr}(\mathbf{K}^2), & \tilde{J}(\xi) \geq 1 \\ 0, & \tilde{J}(\xi) < 1 \end{cases}, \quad \Psi_{\text{bend},3\text{D}}^-(\xi) = \begin{cases} 0, & \tilde{J}(\xi) \geq 1 \\ \xi^2 \frac{12}{T^3} \frac{c}{2} \text{tr}(\mathbf{K}^2), & \tilde{J}(\xi) < 1 \end{cases}. \quad (42)$$

In analogy to Eq. (18.2), the surface stretch \tilde{J} is computed from

$$\tilde{J} = \sqrt{\det[G^{\alpha\beta}] \det[g_{\alpha\beta}]}, \quad (43)$$

where the metrics $G^{\alpha\beta}$ and $g_{\alpha\beta}$ follow from the tangent vectors \mathbf{G}_α and \mathbf{g}_α of the shell layer at points $\mathbf{x} + \xi \mathbf{n}$ and $\mathbf{X} + \xi \mathbf{N}$, respectively (Duong et al., 2017). The resulting moment is given by

$$M^{\alpha\beta} = g(\phi) M_+^{\alpha\beta} + M_-^{\alpha\beta}, \quad (44)$$

with degradation function $g(\phi)$ from Eq. (32) and the contributions

$$M_\pm^{\alpha\beta} = \int_{-\frac{T}{2}}^{\frac{T}{2}} \tilde{M}_\pm^{\alpha\beta}(\xi) d\xi. \quad (45)$$

Here, $\tilde{M}_\pm^{\alpha\beta}$ refers to the split of the moment components stemming from the three-dimensional constitutive law. They are given by

$$\tilde{M}_+^{\alpha\beta} = \begin{cases} \tilde{M}_{\text{bend},3\text{D}}, & \tilde{J}(\xi) \geq 1 \\ 0, & \tilde{J}(\xi) < 1 \end{cases}, \quad \text{and} \quad \tilde{M}_-^{\alpha\beta} = \begin{cases} 0, & \tilde{J}(\xi) \geq 1 \\ \tilde{M}_{\text{bend},3\text{D}}, & \tilde{J}(\xi) < 1 \end{cases}, \quad (46)$$

with $\tilde{M}_{\text{bend},3\text{D}} = \xi^2 \frac{12}{T^3} c (b_0^{\alpha\beta} - B^{\alpha\beta})$ and $b_0^{\alpha\beta} = A^{\alpha\gamma} b_{\gamma\delta} A^{\beta\delta}$.

5 Continuity constraints for patch interfaces

The force vectors of the discretized weak forms in Eqs. (13), (23) and (31) include second-order operators. This necessitates an at least C^1 -continuous discretization⁶. Here, this is obtained by using an isogeometric surface discretization. In general, especially for complex engineering structures, it is not possible to represent the geometry with a single NURBS patch. Instead, multiple patches are required. At the interfaces between these patches, the C^1 -continuity is lost

⁶Unless other methods, like mixed (e.g. displacement and rotation) methods, are used.

and needs to be recovered. For the mechanical shell equations in the weak form from Eqs. (12)–(13), it is sufficient to impose a geometric G^1 -continuity constraint to transfer bending moments across the patch interfaces. Duong et al. (2017) introduce two methods to enforce this constraint for five different edge rotation conditions: enforcing G^1 -continuity, maintaining surface folds, enforcing symmetry conditions on flat sheets, enforcing symmetry conditions on folded sheets and prescribing boundary rotations. Their formulation is summarized and simplified in Sec. 5.1. For the surface concentration and the fracture field, a new C^1 -continuity constraint is proposed in Sec. 5.2. It is used to obtain continuous surface gradients $\nabla_s \phi$ or $\nabla_S \phi$ across patch interfaces. In the present work, conforming meshes are considered and thus, the G^0 - and C^0 -continuity of \mathbf{x} and ϕ are automatically satisfied at the patch interfaces.

In this work, the four different types of patch interfaces depicted in Fig. 2 are considered. From left to right, the number of patches that meet at a point on the surface increases from two to five. The following theory is also valid for other cases, but the examples in Sec. 6 are restricted to the cases depicted in Fig. 2. In the present formulation, a potential that enforces the constraints is added to the total potential of the system, see the subsequent sections. Thus, numerical integration along the patch interfaces is required. These interfaces are shown by the red lines in the figures. The elements meeting at these interfaces are denoted Ω^e , $e = 1, \dots, n_{\text{patch}}$, where n_{patch} denotes the number of patches.

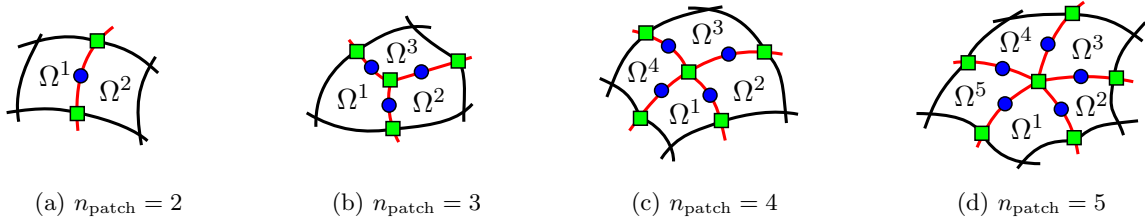


Figure 2: Illustration of different patch constellations. From left to right, the number of patches that share at least one common control point, increases from two to five. The red lines mark the patch interfaces and the elements are denoted Ω^e , $e = 1, \dots, n_{\text{patch}}$. The circular blue and square green symbols mark the position of constant and linear Lagrange multipliers, respectively, along the patch interfaces.

The patch interfaces Γ are discretized into line elements denoted Γ^e that conform to surface elements. Fig. 3 illustrates the local coordinate systems for a given elemental patch interface Γ^e that is parameterized by the coordinate s . Note that the boundary quantities on two adjacent patches are distinguished by a tilde. Both, the interface tangent and normal vector, are

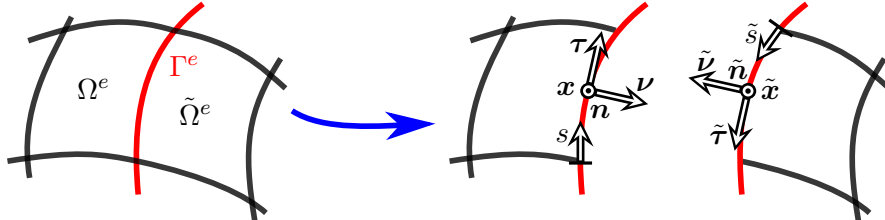


Figure 3: Local coordinate systems $\{\boldsymbol{\nu}, \boldsymbol{\tau}, \boldsymbol{n}\}$ and $\{\tilde{\boldsymbol{\nu}}, \tilde{\boldsymbol{\tau}}, \tilde{\boldsymbol{n}}\}$ at the patch interface Γ^e . Note that the surface normals \boldsymbol{n} and $\tilde{\boldsymbol{n}}$ point out of the paper plane.

orthogonal to the surface normal. They follow from

$$\boldsymbol{\tau} = \frac{\partial \mathbf{x}}{\partial s}, \quad \boldsymbol{\nu} = \boldsymbol{\tau} \times \mathbf{n}, \quad \tilde{\boldsymbol{\tau}} = \frac{\partial \tilde{\mathbf{x}}}{\partial \tilde{s}}, \quad \tilde{\boldsymbol{\nu}} = \tilde{\boldsymbol{\tau}} \times \tilde{\mathbf{n}}, \quad (47)$$

with the relations $\tilde{\mathbf{x}} = \mathbf{x}$ and $\tilde{s} = -s$ for the special case of conforming meshes that are studied in the present work. Hence, $\tilde{\boldsymbol{\tau}} = -\boldsymbol{\tau}$. For the reference configuration, these vectors are defined in analogy to Eq. (47) and are either denoted by a capital letter, or the subscript ‘0’.

The elements Ω^e and $\tilde{\Omega}^e$ share \hat{n}_{CP} control points along the interface Γ^e . These control points are denoted $\hat{\mathbf{x}}_e$ and are used to compute the discretized covariant tangent vector along Γ^e ,

$$\hat{\mathbf{a}}_s \approx \hat{\mathbf{N}}_{,s} \hat{\mathbf{x}}_e, \quad (48)$$

with the shape function array

$$\hat{\mathbf{N}} = [\hat{N}_{i_1} \mathbf{1}, \hat{N}_{i_2} \mathbf{1}, \dots, \hat{N}_{i_{\hat{n}_{\text{CP}}}} \mathbf{1}]. \quad (49)$$

Given $\hat{\mathbf{a}}_s$, the tangent vector $\boldsymbol{\tau}$ is obtained from $\boldsymbol{\tau} = \hat{\mathbf{a}}_s / \|\hat{\mathbf{a}}_s\|$. Its variation is given in Eq. (102.3). Note that other surface quantities on element Ω^e , like the surface normal \mathbf{n} , are obtained from the shape function array $\hat{\mathbf{N}}$ and the nodal values \mathbf{x}_e , see Sec. 2.2. Likewise, these quantities on $\tilde{\Omega}^e$ are obtained from $\tilde{\hat{\mathbf{N}}}$ and $\tilde{\mathbf{x}}_e$.

5.1 G^1 -continuity constraint for the surface deformation

The geometric continuity constraint of Duong et al. (2017) is summarized and simplified in this section. It can be used to enforce the four⁷ different inter-patch conditions shown in Tab. 2. The table distinguishes between the general case of a kink ($\theta \neq \pi$) and the special case of a planar interface ($\theta = \pi$). In both cases either the continuity at patch interfaces or the symmetry at patch boundaries can be enforced. The vectors $\tilde{\mathbf{N}}$ and $\tilde{\mathbf{n}}$ denote the normal of either the neighboring patch or the symmetry plane.

Table 2: Overview of different inter-patch conditions.

	Kink	Planar
Patch interface		
Symmetry condition at a patch boundary		

In the following three subsections, the constraint enforcement for the various cases using the penalty and Lagrange multiplier method are summarized. Their linearizations can be found in Duong et al. (2017).

⁷A fifth possibility is to prescribe boundary rotations, see Duong et al. (2017).

5.1.1 Constraint formulation

As shown in Tab. 2, the general case requires to maintain a fixed angle θ between two adjacent patches. This implies that the angle between the surface normals, which is denoted α , has to be constant for all load or time steps, i.e.

$$\alpha - \alpha_0 = 0, \quad \forall \mathbf{x} \in \Gamma. \quad (50)$$

To avoid the computation and differentiation of the arccos-function, the constraint is reformulated as

$$\cos \alpha - \cos \alpha_0 = 0, \quad \forall \mathbf{x} \in \Gamma, \quad (51)$$

with

$$\cos \alpha := \mathbf{n} \cdot \tilde{\mathbf{n}}, \quad \cos \alpha_0 := \mathbf{N} \cdot \tilde{\mathbf{N}}. \quad (52)$$

Note that Eq. (52) makes use of the fact that the surface normals have unit length. The constraint in Eq. (51) can uniquely handle angles within the range $[0, \pi]$. It leads to the ambiguity in the solution illustrated in Fig. 4. To avoid this ambiguity, a second constraint is incorporated,

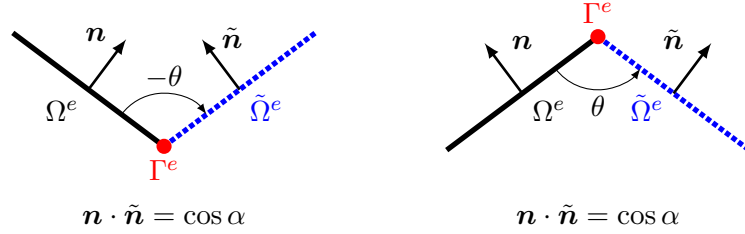


Figure 4: Ambiguity of constraint (51). Both configurations equally fulfill the constraint, which leads to an ambiguity in the numerical solution. If the constraint in Eq. (53) is considered in addition, the desired configuration will be uniquely defined.

i.e.

$$\sin \alpha - \sin \alpha_0 = 0, \quad \forall \mathbf{x} \in \Gamma, \quad (53)$$

where

$$\sin \alpha := (\mathbf{n} \times \tilde{\mathbf{n}}) \cdot \boldsymbol{\tau}, \quad \sin \alpha_0 := (\mathbf{N} \times \tilde{\mathbf{N}}) \cdot \boldsymbol{\tau}_0. \quad (54)$$

Thus, the following set of constraints needs to be enforced

$$\begin{aligned} g_c &:= \cos \alpha_0 - \cos \alpha = 0, \quad \forall \mathbf{x} \in \Gamma, \\ g_s &:= \sin \alpha_0 - \sin \alpha = 0, \quad \forall \mathbf{x} \in \Gamma. \end{aligned} \quad (55)$$

The constraints in Eq. (55) can then uniquely enforce any angle $\alpha_0, \alpha \in [0, 2\pi]$.

Remark: For the planar setting that is illustrated in the third column of Tab. 2, the simplification $\alpha_0 = \alpha = 0$ holds true. Thus, $\cos \alpha_0 = 1$ and $\sin \alpha_0 = 0$. Now, Eq. (55) turns into

$$\begin{aligned} g_c &:= 1 - \cos \alpha = 0, \quad \forall \mathbf{x} \in \Gamma, \\ g_s &:= -\sin \alpha = 0, \quad \forall \mathbf{x} \in \Gamma. \end{aligned} \quad (56)$$

Note that the constraint $g_s = 0$ in Eq. (56) is automatically fulfilled if $g_c = 0$ holds. The two constraints thus simplify to

$$1 - \cos \alpha = 0, \quad \forall \mathbf{x} \in \Gamma, \quad (57)$$

which can also be expressed as

$$\mathbf{g}_n := \mathbf{n} - \tilde{\mathbf{n}} = \mathbf{0}, \quad \forall \mathbf{x} \in \Gamma. \quad (58)$$

5.1.2 Penalty method

For the penalty method, the constraints in Eq. (55) are enforced by adding the potential

$$\Pi_n = \int_{\Gamma_0} \frac{\varepsilon_n}{2} g_n dS = \int_{\Gamma_0} \varepsilon_n (1 - c_0 \cos \alpha - s_0 \sin \alpha) dS, \quad (59)$$

to the total potential of the system. Here, $c_0 := \cos \alpha_0$ and $s_0 := \sin \alpha_0$. The penalty parameter $\varepsilon_n \in (0, \infty)$ controls how well the constraint will be fulfilled. The derivative of the combined constraint $g_n := g_c^2 + g_s^2$ with respect to α reads $g'_n = -\sin(\alpha - \alpha_0)$. The positions of the maxima of g_n , where $g'_n = 0$, fulfill $\alpha - \alpha_0 = \pm\pi$. The minimum is found at $\alpha - \alpha_0 = 0$. A unique solution with the Newton-Raphson method can thus be obtained provided that the initial guess α_i fulfills $|\alpha_i - \alpha_0| < \pi$.

Now, the variation of the penalty potential from Eq. (59) is given by (see Appendix A)

$$\delta\Pi_n = - \int_{\Gamma_0} \varepsilon_n (\delta\boldsymbol{\tau} \cdot \boldsymbol{\theta} + \delta\mathbf{n} \cdot \tilde{\mathbf{d}} + \delta\tilde{\mathbf{n}} \cdot \mathbf{d}) dS, \quad (60)$$

with

$$\boldsymbol{\theta} := s_0 \mathbf{n} \times \tilde{\mathbf{n}} = s_0^2 \boldsymbol{\tau}, \quad \tilde{\mathbf{d}} := c_0 \tilde{\mathbf{n}} + s_0 \tilde{\boldsymbol{\nu}}, \quad \mathbf{d} := c_0 \mathbf{n} + s_0 \boldsymbol{\nu}. \quad (61)$$

Using the variation of $\boldsymbol{\tau}$ given in Eq. (102.3), the first term in the expression for $\delta\Pi_n$ vanishes as $\boldsymbol{\tau} \cdot \delta\boldsymbol{\tau} = 0$. Eq. (60) then simplifies to⁸

$$\delta\Pi_n = - \int_{\Gamma_0} \varepsilon_n (\delta\mathbf{n} \cdot \tilde{\mathbf{d}} + \delta\tilde{\mathbf{n}} \cdot \mathbf{d}) dS. \quad (62)$$

Eq. (60) implies that the bending moments are transmitted exactly across the interface. They are given by $m_\tau = m_{\tilde{\tau}} = \varepsilon_n \sin(\alpha_0 - \alpha)$. The missing variations in Eq. (60) are given in Appendix A. Inserting the FE approximations yields the element-level approximation of Eq. (60)

$$\delta\Pi_n^e := \delta\mathbf{x}_e^T \mathbf{f}_n^e + \delta\tilde{\mathbf{x}}_e^T \mathbf{f}_{\tilde{n}}^e. \quad (63)$$

The elemental force vectors in Eq. (63) are given by

$$\begin{aligned} \mathbf{f}_n^e &:= \int_{\Gamma_0^e} \varepsilon_n \mathbf{N}_{,\alpha}^T (\tilde{\mathbf{d}} \cdot \mathbf{a}^\alpha) \mathbf{n} dS, \\ \mathbf{f}_{\tilde{n}}^e &:= \int_{\Gamma_0^e} \varepsilon_n \tilde{\mathbf{N}}_{,\alpha}^\alpha (\mathbf{d} \cdot \tilde{\mathbf{a}}^\alpha) \tilde{\mathbf{n}} dS, \end{aligned} \quad (64)$$

with shape function array \mathbf{N} from Eq. (9) and Γ_0^e denoting a finite line element along the patch interface. The force vectors \mathbf{f}_n^e and $\mathbf{f}_{\tilde{n}}^e$ have dimension $3n_e \times 1$ and $3n_{\tilde{e}} \times 1$, respectively. Here, n_e and $n_{\tilde{e}}$ refer to the number of control points associated with the elements Ω^e and $\tilde{\Omega}^e$, respectively.

Remark: Plugging in $\alpha_0 = 0$ into the force vectors in Eq. (64), leads to the simplified force vectors

$$\begin{aligned} \mathbf{f}_n^e &:= \int_{\Gamma_0^e} \varepsilon_n \mathbf{N}_{,\alpha}^T (\tilde{\mathbf{n}} \cdot \mathbf{a}^\alpha) \mathbf{n} dS = \int_{\Gamma_0^e} \varepsilon_n \mathbf{N}_{,\alpha}^T (\mathbf{n} \otimes \tilde{\mathbf{n}}) \mathbf{a}^\alpha dS, \\ \mathbf{f}_{\tilde{n}}^e &:= \int_{\Gamma_0^e} \varepsilon_n \tilde{\mathbf{N}}_{,\alpha}^\alpha (\mathbf{n} \cdot \tilde{\mathbf{a}}^\alpha) \tilde{\mathbf{n}} dS = \int_{\Gamma_0^e} \varepsilon_n \tilde{\mathbf{N}}_{,\alpha}^\alpha (\tilde{\mathbf{n}} \otimes \mathbf{n}) \tilde{\mathbf{a}}^\alpha dS, \end{aligned} \quad (65)$$

for the penalty method.

⁸This is a simplification compared to the formulation of Duong et al. (2017).

5.1.3 Lagrange multiplier method

For the Lagrange multiplier approach, the constraints in Eq. (55) are reformulated as follows

$$\begin{aligned}\bar{g}_c &:= 1 - \cos(\alpha - \alpha_0) = 0, \\ \bar{g}_s &:= \sin(\alpha - \alpha_0) = 0,\end{aligned}\tag{66}$$

to guarantee unique solutions with the Newton-Raphson method as long as $|\alpha_i - \alpha_0| < \pi/4$, with initial guess α_i . The new potential then is

$$\Pi_n = \int_{\Gamma_0} q (\bar{g}_c + \bar{g}_s) dS = \int_{\Gamma_0} q (1 - \cos(\alpha - \alpha_0) + \sin(\alpha - \alpha_0)) dS,\tag{67}$$

with Lagrange multiplier q . Both potentials in Eqs. (59) and (67) have their minimum at $\alpha = \alpha_0$. Using Eqs. (100)–(101), the variation of the Lagrange multiplier potential in Eq. (67) is given by

$$\delta\Pi_n = \int_{\Gamma_0} \delta q (\bar{g}_c + \bar{g}_s) dS - \int_{\Gamma_0} q (\delta\boldsymbol{\tau} \cdot \boldsymbol{\theta} + \delta\mathbf{n} \cdot \tilde{\mathbf{d}} + \delta\tilde{\mathbf{n}} \cdot \mathbf{d}) dS,\tag{68}$$

with the redefinitions

$$\boldsymbol{\theta} := (s_0 - c_0) \mathbf{n} \times \tilde{\mathbf{n}}, \quad \mathbf{d} := (s_0 + c_0) \mathbf{n} + (s_0 - c_0) \boldsymbol{\nu}, \quad \tilde{\mathbf{d}} := (s_0 + c_0) \tilde{\mathbf{n}} + (s_0 - c_0) \tilde{\boldsymbol{\nu}}.\tag{69}$$

Eq. (68) simplifies to⁸

$$\delta\Pi_n = \int_{\Gamma_0} \delta q (\bar{g}_c + \bar{g}_s) dS - \int_{\Gamma_0} q (\delta\mathbf{n} \cdot \tilde{\mathbf{d}} + \delta\tilde{\mathbf{n}} \cdot \mathbf{d}) dS,\tag{70}$$

since $\boldsymbol{\tau} \cdot \delta\boldsymbol{\tau} = 0$, see previous section. Eq. (68) implies that the bending moment $m_\tau = m_{\tilde{\tau}} = -q$ is transmitted exactly across the patch interface. The FE approximation of the Lagrange multiplier along Γ^e can be written as

$$q \approx \mathbf{N}_q \mathbf{q}_e,\tag{71}$$

where \mathbf{N}_q and \mathbf{q}_e are the corresponding shape function array and nodal values of line element Γ^e , respectively. The positions of these nodal values for different order of interpolation are illustrated in Fig. 2. The discretized element-level variation of the Lagrange multiplier potential is

$$\delta\Pi_n^e = \delta\mathbf{x}_e^T \mathbf{f}_n^e + \delta\tilde{\mathbf{x}}_e^T \mathbf{f}_{\tilde{n}}^e + \delta\mathbf{q}_e^T \mathbf{f}_q^e,\tag{72}$$

with the new force vector

$$\bar{\mathbf{f}}_q^e := \int_{\Gamma_0^e} \mathbf{N}_q^T (\bar{g}_c + \bar{g}_s) dS.\tag{73}$$

The force vectors $\bar{\mathbf{f}}_n^e$ and $\bar{\mathbf{f}}_{\tilde{n}}^e$ in Eq. (72) are the same as in Eq. (64) with the substitutions $\varepsilon_n \leftarrow 1$, $c_0 \leftarrow q(s_0 + c_0)$, $s_0 \leftarrow q(s_0 - c_0)$ and the variables \mathbf{d} and $\tilde{\mathbf{d}}$ being defined as in Eq. (69). The force vectors $\bar{\mathbf{f}}_n^e$ and $\bar{\mathbf{f}}_{\tilde{n}}^e$ have dimension $3n_e \times 1$ and $3n_{\tilde{e}} \times 1$, respectively. Here, n_e and $n_{\tilde{e}}$ refer to the number of control points associated with the elements Ω^e and $\tilde{\Omega}^e$, respectively. Further, $\bar{\mathbf{f}}_q^e$ has dimension $n_q \times 1$ with n_q denoting the number of Lagrange multipliers on the line element Γ^e , see Fig. 2.

Remark: For the simplified constraint in Eq. (58), the force vectors $\bar{\mathbf{f}}_n^e$ and $\bar{\mathbf{f}}_{\tilde{n}}^e$ in Eq. (63) are simplified in analogy to the force vectors from the penalty method, see Eq. (65). Again, the substitutions $\varepsilon_n \leftarrow 1$, $c_0 \leftarrow q$ and $s_0 \leftarrow -q$ have to be inserted. The force vector $\bar{\mathbf{f}}_q^e$ in Eq. (73) stays the same.

5.2 C^1 -continuity constraint for the phase field

This section discusses the formulations to enforce C^1 -continuity for the phase fields ϕ , see Eqs. (23) and (31). The linearizations are outlined in Appendix B.

5.2.1 Constraints for the phase field

As Fig. 5 illustrates, the surface gradients of the phase field, $\nabla_s \phi$ and $\nabla_s \tilde{\phi}$, need to be equal to ensure C^1 -continuity of ϕ . The constraint can thus be written as

$$\nabla_s \phi - \nabla_s \tilde{\phi} = \mathbf{0}, \quad \forall \mathbf{x} \in \Gamma. \quad (74)$$

The parameterization of the elements $\tilde{\Omega}^e$ and Ω^e is the same along the interface because here, conforming meshes are considered, see Fig. 3. Thus, by construction, the tangential component

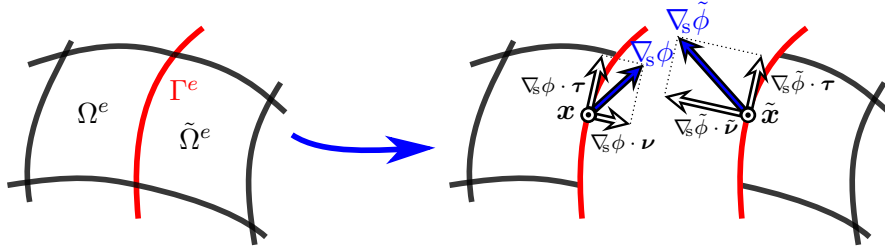


Figure 5: Surface gradients $\nabla_s \phi$ and $\nabla_s \tilde{\phi}$ at points \mathbf{x} and $\tilde{\mathbf{x}}$, respectively. Due to conforming meshes at the interface Γ^e , the parameterization along the interface is the same for both patches. Thus, the tangential component of the surface gradients is equal by construction, i.e. $\nabla_s \phi \cdot \boldsymbol{\tau} = \nabla_s \tilde{\phi} \cdot \boldsymbol{\tau}$. Only their normal components need to be enforced to be equal, see Eq. (75).

of $\nabla_s \phi$ is C^1 -continuous across the patch interface. Hence, only its normal component needs to be enforced to be equal. The constraint in Eq. (74) then simplifies to

$$g_\nabla := \nabla_s \phi \cdot \boldsymbol{\nu} + \nabla_s \tilde{\phi} \cdot \tilde{\boldsymbol{\nu}} = 0, \quad \forall \mathbf{x} \in \Gamma. \quad (75)$$

It has the unit $[\text{m}^{-1}]$. In the case of fracture, the gradients are evaluated in the reference configuration, and hence constraint (75) is rewritten as

$$g_\nabla := \nabla_S \phi \cdot \boldsymbol{\nu}_0 + \nabla_S \tilde{\phi} \cdot \tilde{\boldsymbol{\nu}}_0 = 0, \quad \forall \mathbf{x} \in \Gamma. \quad (76)$$

Based on Eq. (6.1), Eq. (75) can be rewritten as

$$g_\nabla = \phi_{,\alpha} \mathbf{a}^\alpha \cdot \boldsymbol{\nu} + \tilde{\phi}_{,\beta} \tilde{\mathbf{a}}^\beta \cdot \tilde{\boldsymbol{\nu}} = 0, \quad \forall \mathbf{x} \in \Gamma. \quad (77)$$

Keeping \mathbf{x} fixed, the variation of Eq. (77) is given by

$$\delta g_\nabla = \delta \phi_{,\alpha} \mathbf{a}^\alpha \cdot \boldsymbol{\nu} + \delta \tilde{\phi}_{,\beta} \tilde{\mathbf{a}}^\beta \cdot \tilde{\boldsymbol{\nu}}. \quad (78)$$

Keeping \mathbf{x} fixed is sufficient for building a numerical method, even though it introduces a variational inconsistency as is noted below. The reason is that constraint (77) is used for the phase field, and not for the displacement field. Thus, the latter can be fixed in the variation and hence, Eq. (78) does not include the variations of the tangent vectors \mathbf{a}^α , $\tilde{\mathbf{a}}^\beta$ or the interface normals $\boldsymbol{\nu}$, $\tilde{\boldsymbol{\nu}}$, which simplifies the numerical formulations greatly. The linearization of g_∇ , however, needs to include the linearizations with respect to \mathbf{x} , see Appendix B.1, in order to

ensure quadratic convergence of the Newton-Raphson method. Based on the FE approximations in Eq. (10) and the analogous quantities for $\tilde{\phi}$, the variation of the constraint in Eq. (78) is discretized as

$$\delta g_{\nabla} \approx \delta \phi_e^T \bar{\mathbf{N}}_{,\alpha}^T (\mathbf{a}^\alpha \cdot \boldsymbol{\nu}) + \delta \tilde{\phi}_e^T \tilde{\mathbf{N}}_{,\beta}^T (\tilde{\mathbf{a}}^\beta \cdot \tilde{\boldsymbol{\nu}}), \quad (79)$$

where the tangent vectors and interface normals are also understood to be discrete.

Remark: In the case of planar connections of patches, the relation $\mathbf{n} = \tilde{\mathbf{n}}$ can be used, see Eq. (58). From Eq. (47) it then follows that $\boldsymbol{\nu} = -\tilde{\boldsymbol{\nu}}$. The general constraint in Eq. (77) now simplifies to

$$g_{\nabla}^{\text{planar}} = \left(\phi_{,\alpha} \mathbf{a}^\alpha - \tilde{\phi}_{,\beta} \tilde{\mathbf{a}}^\beta \right) \cdot \boldsymbol{\nu} = 0, \quad \forall \mathbf{x} \in \Gamma. \quad (80)$$

Its variation is then given by

$$\delta g_{\nabla}^{\text{planar}} = \left(\delta \phi_{,\alpha} \mathbf{a}^\alpha - \delta \tilde{\phi}_{,\beta} \tilde{\mathbf{a}}^\beta \right) \cdot \boldsymbol{\nu}. \quad (81)$$

The following section discuss a penalty and a Lagrange multiplier approach to enforce these constraints. Both methods are based on a potential Π_{∇} that is added to the system's total potential. Its variation and discretization will be outlined. Their linearization is derived in Appendix B.

Remark: In the present work, only planar connections are considered the for phase separation examples in Sec. 6.2. In contrast, the fracture examples in Sec. 6.3 include the more general case of non-smooth connections between patches. But for fracture, the phase field gradient is based on the reference configuration. To cover all cases, the following derivations only contain the general case.

5.2.2 Penalty method

In analogy to the penalty potential for the G^1 -constraint, see Eq. (59), the penalty potential for the phase field constraint in Eq. (77) is given by

$$\Pi_{\nabla} = \int_{\Gamma_0} \frac{\varepsilon_{\phi}}{2} g_{\nabla}^2 dS, \quad (82)$$

where the penalty parameter $\varepsilon_{\phi} \in (0, \infty)$ with units $[\text{kg m}^3/\text{s}^2]$ controls how well the constraint will be fulfilled. The variation of Π_{∇} is

$$\delta \Pi_{\nabla} = \int_{\Gamma_0} \varepsilon_{\phi} g_{\nabla} \delta g_{\nabla} dS, \quad (83)$$

where δg_{∇} is given in Eq. (78).⁹ Based on Eq. (79), the discretized variation of the penalty potential becomes

$$\delta \Pi_{\nabla}^e = \delta \phi_e^T \mathbf{f}_{\phi}^e + \delta \tilde{\phi}_e^T \mathbf{f}_{\tilde{\phi}}^e. \quad (84)$$

The general force vectors in Eq. (84) are given by

$$\begin{aligned} \mathbf{f}_{\phi}^e &:= \int_{\Gamma_0^e} \varepsilon_{\phi} \bar{\mathbf{N}}_{,\alpha}^T g_{\nabla} (\mathbf{a}^\alpha \cdot \boldsymbol{\nu}) dS, \\ \mathbf{f}_{\tilde{\phi}}^e &:= \int_{\Gamma_0^e} \varepsilon_{\phi} \tilde{\mathbf{N}}_{,\alpha}^T g_{\nabla} (\tilde{\mathbf{a}}^\alpha \cdot \tilde{\boldsymbol{\nu}}) dS, \end{aligned} \quad (85)$$

with g_{∇} from Eq. (77).

⁹Since \mathbf{x} is kept fixed in δg_{∇} , Eq. (83) is not the full variation of Π_{∇} .

The choice of the penalty parameter

Based on numerical investigations, the following penalty parameter for phase separations is used

$$\varepsilon_\phi = \varepsilon_\phi^0 2^{d(p-1)}, \quad (86)$$

with $\varepsilon_\phi^0 = 500 N\omega L_0$. Here, L_0 refers to a reference length stemming from a dimensionless form (cf. Sec. 6.2 and Zimmermann et al. (2019)). The polynomial order of the discretization is p and the refinement depth is denoted d . According to Eq. (86), finer meshes will lead to a larger penalty parameter.

For brittle fracture, following problem-independent penalty parameter is proposed

$$\varepsilon_\phi = \varepsilon_\phi^0 \Delta x_{\min}^\Gamma \frac{\Delta t}{\Delta t_{\max}} \left(\frac{\Delta x_{\max}^\Gamma}{\Delta x} \right)^d, \quad (87)$$

with $\varepsilon_\phi^0 = 0.1 E_0 L_0^2$. The reference stiffness E_0 ($[N/m] = [kg/s^2]$) and length L_0 ($[m]$) stem from the non-dimensionization scheme described in Paul et al. (2019). Δx_{\min}^Γ and Δx_{\max}^Γ refer to the minimum and maximum length of the line elements along the patch interfaces, respectively, whereas Δx refers to the one from the currently considered line element. The penalty parameter is thus, increased in regions of more resolved meshes, where fracture occurs. The maximum refinement depth d enhances this effect. Ill-conditioning stemming from too large penalty parameters is prevented by scaling ε_ϕ with Δx_{\min}^Γ . The scaling by the time step Δt leads to larger penalty parameters in the case that large time steps are used. Note that the strong form is multiplied with the factor $2\ell_0/\mathcal{G}_c$ in the phase field framework (Paul et al., 2019). The penalty parameter is thus, implicitly scaled with this factor. The value $\varepsilon_\phi^0 = 0.1 E_0 L_0^2$ seems small, but it yields sufficiently accurate results, see Sec. 6.3.

5.2.3 Lagrange multiplier method

In the following, a Lagrange multiplier approach to enforce constraint (77) is described. Since both of these constraints are scalar, the additional potential reads

$$\Pi_\nabla = \int_{\Gamma_0} \lambda g_\nabla dS, \quad (88)$$

with Lagrange multiplier λ . The variation of potential (88) is

$$\delta \Pi_\nabla = \int_{\Gamma_0} \delta \lambda g_\nabla dS + \int_{\Gamma_0} \lambda \delta g_\nabla dS, \quad (89)$$

where δg_∇ is given in Eq. (78). The FE approximations of the Lagrange multiplier and its variation are

$$\lambda \approx \mathbf{N}_\lambda \boldsymbol{\lambda}_e, \quad \text{and} \quad \delta \lambda \approx \mathbf{N}_\lambda \delta \boldsymbol{\lambda}_e, \quad (90)$$

with shape function array

$$\mathbf{N}_\lambda := [N_{i_1}], \quad \text{or} \quad \mathbf{N}_\lambda := [N_{i_1}, N_{i_2}], \quad (91)$$

depending on the order of interpolation (constant or linear, respectively). The nodal values of the Lagrange multiplier and their variation are denoted $\boldsymbol{\lambda}_e$ and $\delta \boldsymbol{\lambda}_e$, respectively. Using the FE approximation of $\delta \lambda$ from Eq. (90) and of δg_∇ from Eq. (79), the discretized variation of the Lagrange multiplier potential becomes

$$\delta \Pi_\nabla^e = \delta \boldsymbol{\phi}_e^T \bar{\mathbf{f}}_\phi^e + \delta \tilde{\boldsymbol{\phi}}_e^T \bar{\mathbf{f}}_\phi^e + \delta \boldsymbol{\lambda}_e^T \mathbf{f}_\lambda^e. \quad (92)$$

The general force vectors in Eq. (92) are given by

$$\begin{aligned}\bar{\mathbf{f}}_\phi^e &:= \int_{\Gamma_0^e} \bar{\mathbf{N}}_{,\alpha}^T \lambda (\mathbf{a}^\alpha \cdot \boldsymbol{\nu}) \, dS, \\ \bar{\mathbf{f}}_\phi^e &:= \int_{\Gamma_0^e} \tilde{\bar{\mathbf{N}}}_{,\alpha}^T \lambda (\tilde{\mathbf{a}}^\alpha \cdot \tilde{\boldsymbol{\nu}}) \, dS, \\ \bar{\mathbf{f}}_\lambda^e &:= \int_{\Gamma_0^e} \mathbf{N}_\lambda^T g_\nabla \, dS,\end{aligned}\tag{93}$$

with g_∇ from Eq. (77).

6 Numerical examples

This section shows several numerical examples that illustrate the influence of the patch constraints from Sec. 5 on the numerical solution. At first, Sec. 6.1 focuses on the pure shell framework and the influence of the G^1 -continuity constraint from Sec. 5.1. Secondly, phase transitions on multi-patch geometries for thin shells are investigated in Sec. 6.2. Similar investigations are made for brittle fracture in Sec. 6.3.

In the subsequent sections, the following notation is used: The surface consists of n_{patch} patches, which are discretized by n_{el} surface elements and n_{CP} control points, excluding the discretization of the patch interfaces. The penalty method is abbreviated by PM and the Lagrange multiplier method with constant/linear interpolation by constant/linear LMM.

Remark: Integration over the line elements Γ_0^e is performed using Gaussian quadrature. The choice of quadrature rules might have an influence on overconstraining and locking, which is not investigated here. Instead, these topics are left for future work.

6.1 Deforming shells

This section investigates the G^1 -continuity constraint from Sec. 5.1 within the pure mechanical shell framework (where ϕ is not unknown). The discussion includes comparisons to given solutions and convergence rates. To obtain an analytical reference solution, the examples in this section are based on quasi-static conditions and assume linear elastic material behavior.

6.1.1 Pure bending

First, the pure bending of an initially flat shell is considered. The setup is depicted in Figs. 6a and 7a for different number of patches. As shown, an external bending moment M is applied at the two opposite edges to obtain pure bending. Figs. 6b and 7b shows the relative error of the mean curvature H in comparison to the analytical solution given in Sauer and Duong (2017). Fig. 8 shows the L_2 - and maximum displacement error for an increasing number of elements. For reference, the error decay for an increasing number of elements using a single patch is shown. In contrast to the penalty method, the Lagrange multiplier method performs better with respect to the L_2 -error, both, in absolute value and convergence rate. No difference between constant and linear interpolation of the Lagrange multipliers can be observed. This is due to the fact that the bending moment is constant everywhere. Hence, a constant Lagrange multiplier interpolation is sufficient. The maximum displacement error shows no noticeable difference between the Lagrange multiplier and penalty method.

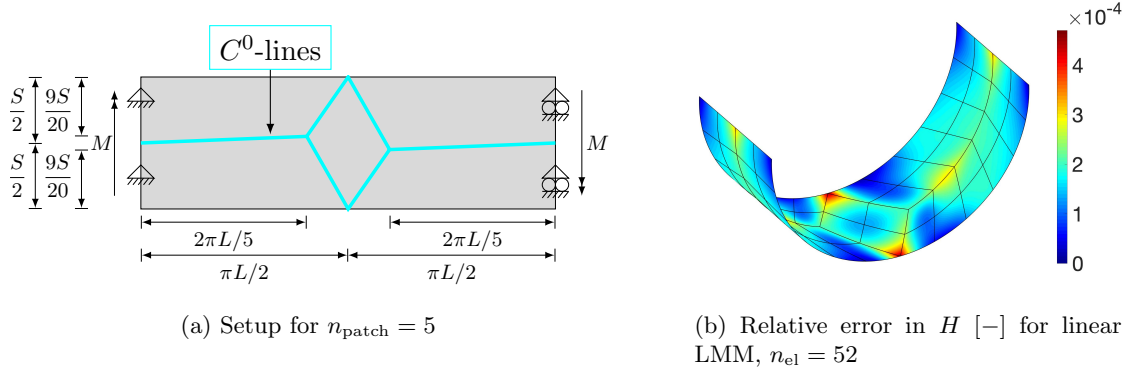


Figure 6: Pure bending: (a) Five-patch geometry (the out-of-plane movement is prohibited at the left and right edge) and (b) relative error in the mean curvature H plotted over the deformed configuration.

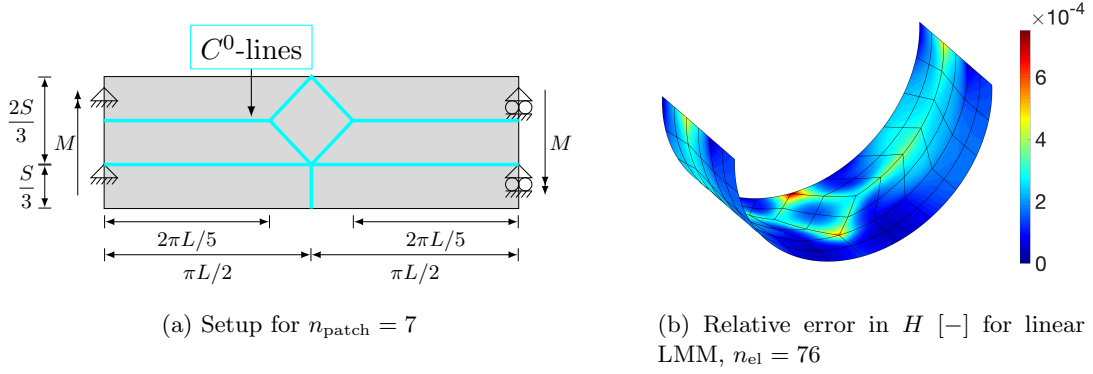


Figure 7: Pure bending: (a) Seven-patch geometry (the out-of-plane movement is prohibited at the left and right edge) and (b) relative error in the mean curvature H plotted over the deformed configuration.

6.1.2 Pinching of a hemisphere

This section investigates the pinching of a hemisphere. The setup consists either of a single degenerated patch or three patches as is illustrated in Fig. 9. Along the vertical edges, the symmetry constraint for smooth patch connections is enforced by the Lagrange multiplier method using constant interpolation. External forces of magnitude $F = 2 E_0 L_0$ act on the lower corners, see Fig. 9. The problem is normalized by the unit length L_0 and the unit stiffness E_0 (measured as force/length).

Fig. 10 shows the normalized displacement over the number of elements. It is measured under the points loads and the reference displacement is $0.0924 L_0$ (Morley and Morris, 1978; Belytschko et al., 1985; Macneal and Harder, 1985). The black line marks the reference solution using a single-patch discretization. Good convergence is obtained, except for the case, when the constraint is not enforced. The red dashed line converges to a slightly larger value.

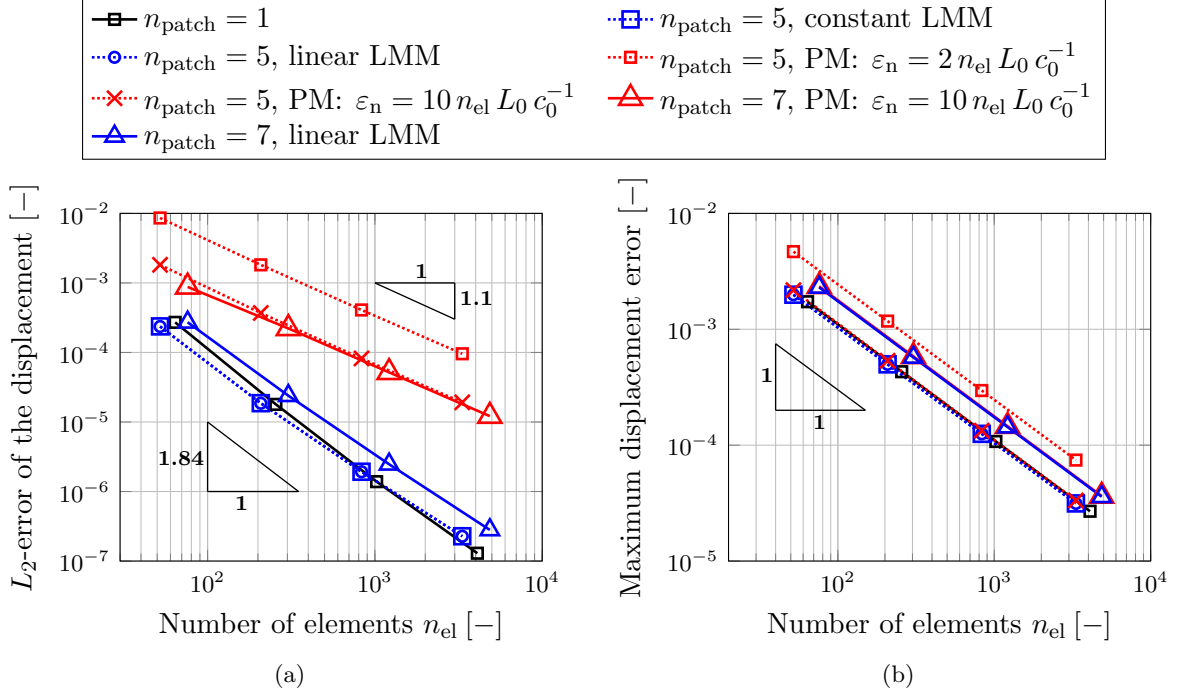


Figure 8: Pure bending: Convergence of the proposed method with respect to (a) the L_2 -error of the displacement and (b) the maximum displacement error. The penalty parameter is normalized by the unit length L_0 and the unit bending stiffness c_0 .

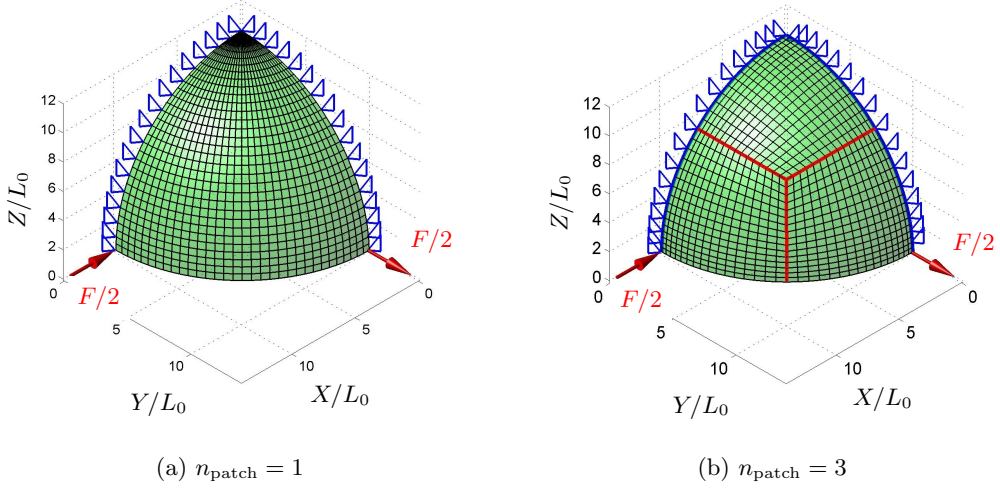


Figure 9: Pinching of a hemisphere: Discretizations of a quarter model using (a) a single-patch or (b) three patches. The red lines mark the patch interfaces. The blue lines mark the interfaces where symmetry is enforced.

6.2 Phase separation on deforming shells

This section investigates phase separation according to the theory from Sec. 3. The color coding of the phase field follows a blue ($\phi = 0$) to red ($\phi = 1$) transition, see Fig. 1a. For the examples in this section, the simplified phase field constraint for the special case of planar patch connections

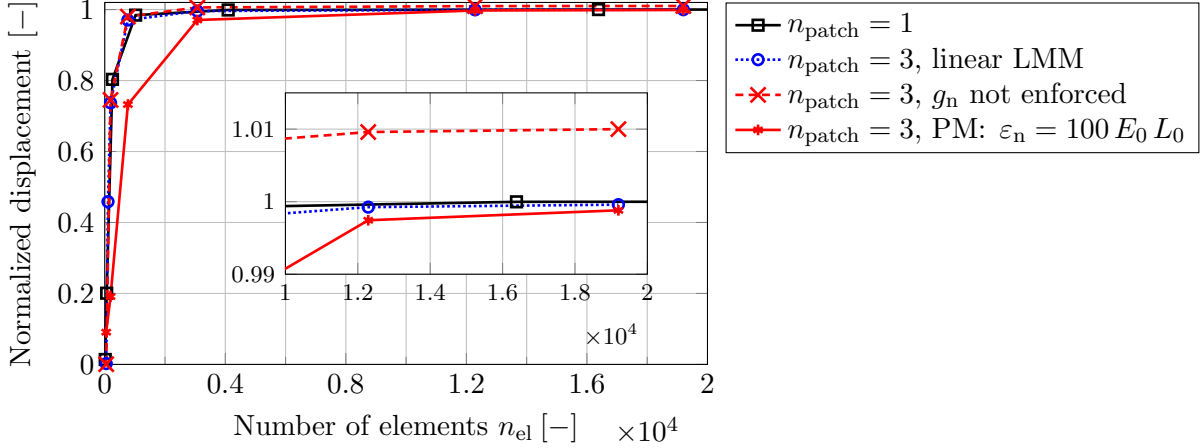


Figure 10: Pinching of a hemisphere: Normalized displacement over the mesh refinement.

is used, see Eq. (80). In all examples, the initial concentration field is set to

$$\phi(\xi^\alpha, 0) = \bar{\phi} + \phi_r(\xi^\alpha), \quad (94)$$

with $\bar{\phi} = 1/3$ and random distribution $\phi_r \in [-0.05, 0.05]$, if not stated otherwise. The mechanical material parameters are given in Table 3 with 2D Young's modulus $E = N\omega$ and Poisson's ratio $\nu = 0.3$. All quantities are dimensionless by the introduction of a reference length L_0 ,

Table 3: Material parameters for the phase separation examples.

	Pure phase state $\phi = 0$ (blue color)	Pure phase state $\phi = 1$ (red color)
K_i	$K_0 = 1.25 \frac{E \nu}{(1 + \nu)(1 - 2 \nu)}$	$K_1 = 0.0375 \frac{E \nu}{(1 + \nu)(1 - 2 \nu)}$
G_i	$G_0 = 6.25 \frac{E}{2(1 + \nu)}$	$G_1 = 0.375 \frac{E}{2(1 + \nu)}$
c_i	$c_0 = 0.01 E L_0$	$c_1 = 0.0001875 E L_0$
η_i	$\eta_0 = 1.5 K_0 T_0$	$\eta_1 = 1.5 K_0 T_0$

time T_0 and energy density Ψ_0 . From this, a reference stiffness E_0 and density $\rho_0 = T_0^2 \Psi_0 / L_0^2$ follow (Zimmermann et al., 2019). Further, $N\omega = \Psi_0$ and $Nk_B T = \Psi_0/3$.

6.2.1 Pressurized torus

This section investigates phase separation on a torus, which is subjected to the constant internal pressure $p = 0.09 E_0 L_0^{-1}$. The geometry is shown in Fig. 11a. The major and minor radii are $1.3 L_0$ and $0.2 L_0$, respectively. The length scale parameter is $\ell = \sqrt{0.075} L_0$. The cyan-colored line shows a patch interface, where the surface discretization is only C^0 -continuous. Given a continuous parametrization of the torus, the C^0 -line is obtained by knot insertion at the respective position in the global knot vector. Figs. 11b–11c illustrate the evolution of the phase field and the mechanical deformation using constant Lagrange multipliers for both the constraints in Eqs. (66) and (80), and using a mesh consisting of $n_{CP} = 4128$ control points. The results show good agreement with the results stemming from an overall C^1 -continuous discretization with $n_{CP} = 4096$ control points. This is illustrated in Fig. 12, where the relative

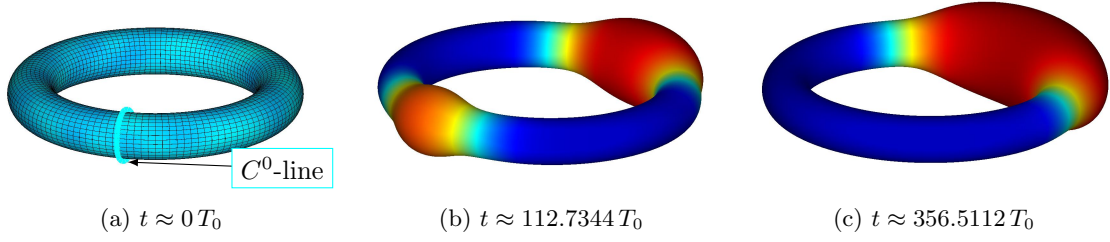


Figure 11: Pressurized torus: (a) Geometry with a C^0 -line (marked by the bold cyan-colored line), and (b)–(c) evolution of the phase field and mechanical deformation for the case that the constraints are fulfilled with the Lagrange multiplier method using constant interpolation.

error of the Cahn-Hilliard energy is plotted over time.¹⁰ The enforcement of the continuity constraints using the penalty method shows similarly good results. The black dash-dotted line reflects the relative error when the continuity constraints are not enforced. As a result of this insufficient discretization, the error is several orders of magnitude larger compared to the results without constraint enforcement. Fig. 13 visualizes the deformed configuration for the case that

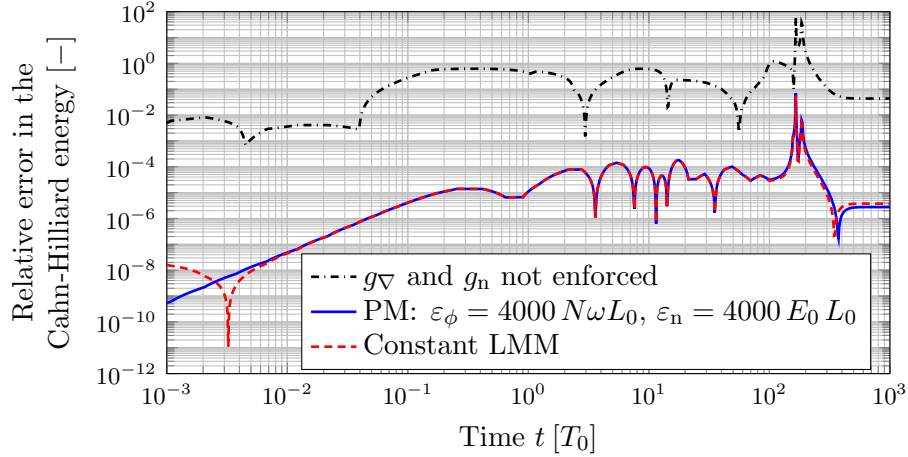


Figure 12: Pressurized torus: Relative error of the Cahn-Hilliard energy over time. The results from an overall C^1 -continuous discretization with $n_{CP} = 4096$ control points are used as a reference solution.¹⁰ The used penalty parameter ε_ϕ is equal to the one proposed in Eq. (86).

the constraints are not enforced. Already at early times, the insufficient discretization leads to kinks in the geometry that attract phase separation, see Fig. 13a and its enlargement in Fig. 13b. Also, the stresses show non-physical peaks at the C^0 -line, see Fig. 13c. Here, the elastic surface tension is

$$\gamma_{el} = \frac{1}{2} N_{el}^{\alpha\beta} a_{\alpha\beta}, \quad (95)$$

where $N_{el}^{\alpha\beta}$ denotes the elastic Cauchy stress components (Sauer and Duong, 2017). The wrong result at early times leads to a different final state. Thus, the relative error of the Cahn-Hilliard energy is much higher for the unconstrained problem, see Fig. 12.

¹⁰The time steps of the two simulations are not coinciding. Therefore, the energy is linearly interpolated between the time steps to compute the relative energy difference.

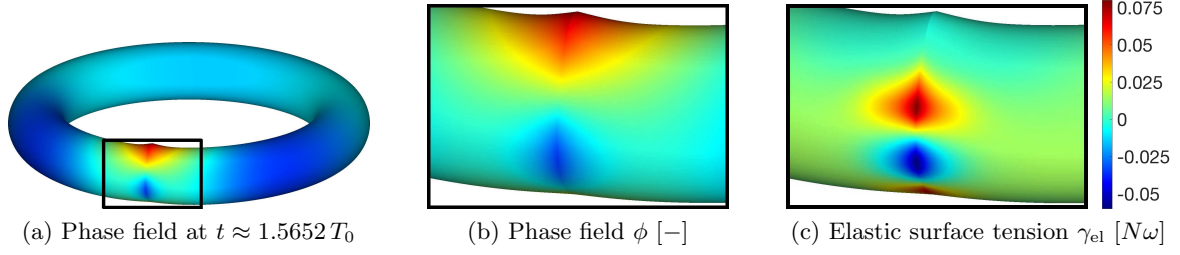


Figure 13: Pressurized torus: (a) Phase field at early times when no constraints are enforced; Enlargement of (b) phase field and (c) elastic surface tension. The insufficient discretization leads to the formation of kinks, non-physical phase separation and stress peaks.

6.2.2 Phase separation on a deforming sphere

This section investigates phase separation on a spherical shell. It is either discretized by six patches, see Fig. 14a, or by unstructured cubic splines, see Fig. 14b. The latter serves as reference as it provides C^2 -continuity everywhere except for eight so-called extraordinary points, where only C^1 -continuity is maintained (Toshniwal et al., 2017).

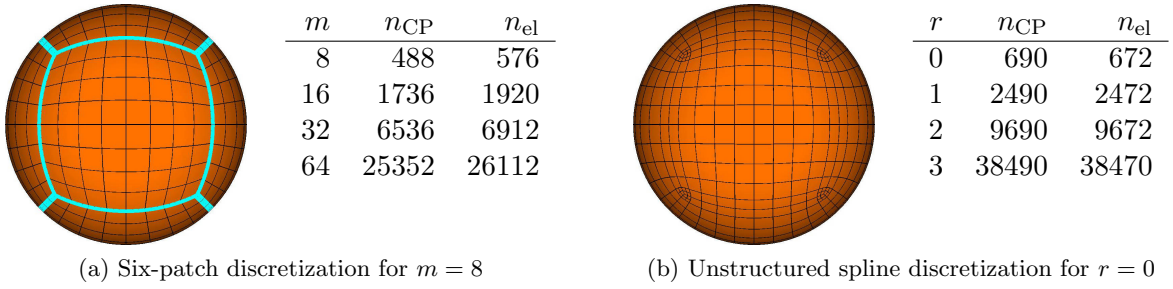


Figure 14: Spline discretizations of a sphere and corresponding mesh properties for different refinement levels for (a) the six-patch discretization (the bold cyan-colored lines mark the patch interfaces) and (b) an unstructured spline discretization.

First, this section investigates the phase field evolution on a sphere for the interface parameter $\ell = \sqrt{0.001} L_0$. The initial radius of the sphere is L_0 and the constant pressure $p = 0.04 E_0 L_0^{-1}$ is applied to its interior surface. The mobility constant is $D = 2.5 T_0$. Fig. 15 shows several snapshots for the phase separation for the six-patch discretization with $m = 64$ in the first row, and the unstructured spline discretization with $r = 3$ in the second row. Both show excellent agreement in space and time. Due to the small interface parameter, multiple red phase nuclei appear. As the time progresses, these bulge, merge and evolve. The deformation is larger at locations where the nuclei grow. In Fig. 16, the elastic and viscous surface tensions are shown for the two different discretization techniques. The viscous surface tension γ_{visc} follows in analogy to Eq. (95) from the viscous Cauchy stress. The largest values of the elastic surface tension are obtained around the evolving bulges, while the smallest are in their center. Viscous effects are comparatively large at disappearing and around growing bulges. Again, both results from the different discretization techniques show excellent agreement.

Second, the results from the two discretization approaches are compared for the case that an internal pressure of $p = 0.04 E_0 L_0^{-1}$ is imposed on the initially undeformed sphere and the

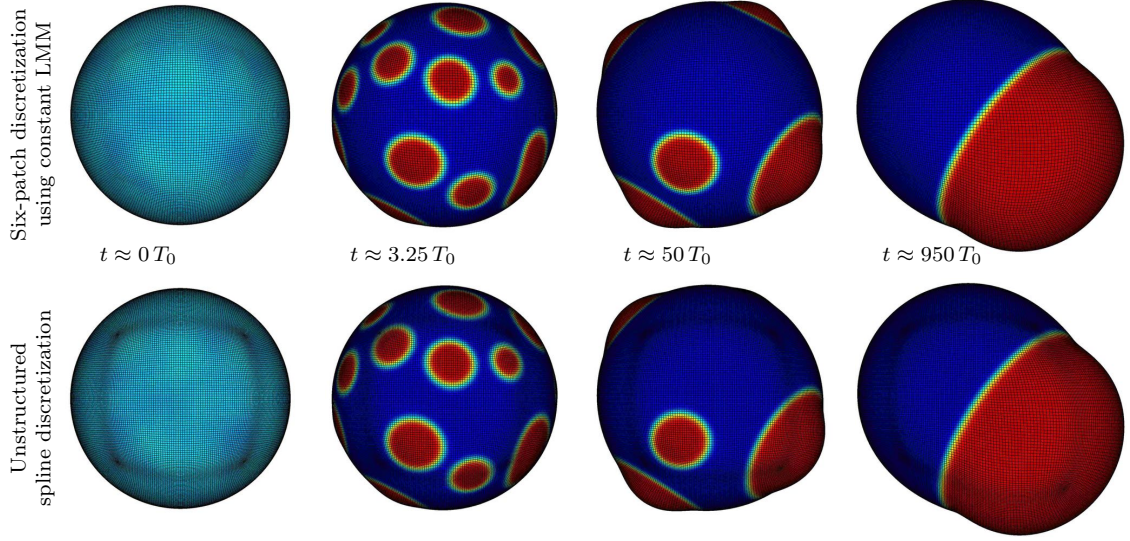


Figure 15: Phase separation on a deforming sphere: The top row shows the phase evolution for the six-patch discretization, the bottom row for the unstructured spline discretization. The constraints for the first one are enforced by the Lagrange multiplier method with constant interpolation. Both cases show excellent agreement.

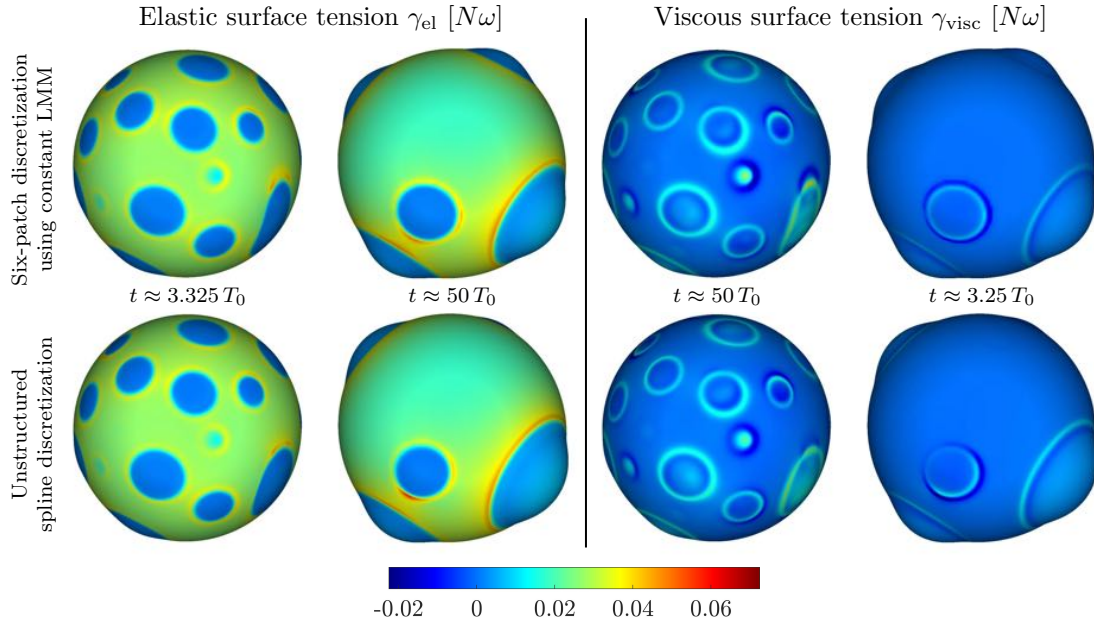


Figure 16: Phase separation on a deforming sphere: The top row shows the elastic and viscous surface tensions for the six-patch discretization, the bottom row for the unstructured spline discretization. The constraints for the first one are enforced by the Lagrange multiplier method with constant interpolation. Both cases show excellent agreement.

initial concentration field is

$$\phi(\xi^\alpha, 0) = \begin{cases} 1/2, & z \geq 0 \\ 1/6, & z < 0 \end{cases}. \quad (96)$$

The interface parameter is now set to $\ell = \sqrt{0.05} L_0$. The final deformation and phase distribution is visualized on the inset of Fig. 17. Next to it, the black dotted line shows the phase field value over the height-coordinate of the illustrated cutting plane for the unstructured spline discretization with $r = 0$ (see Fig. 14b). Further, the elastic surface tension for different refinement levels m and r (see Fig. 14) is illustrated in Fig. 17. For an increasing number of control points, the results from the six-patch discretization and the unstructured spline discretization converge. This shows that the proposed patch constraints successfully enforce continuity for the coupled problem.

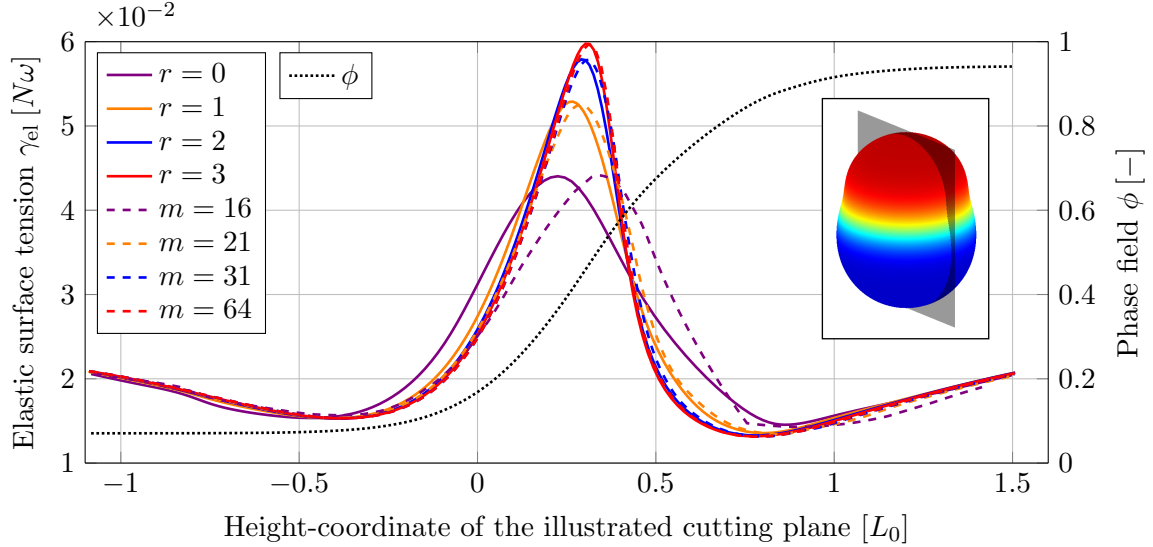


Figure 17: Phase separation on a deforming sphere: Final deformation and phase distribution for the initial state in Eq. (96). Surface tension (left axis) and phase field (right axis) over the height-coordinate for the six-patch discretization (variable m) and the unstructured spline discretization (variable r). The results of the two discretization techniques converge for an increasing number of control points.

6.3 Fracture of deforming shells

This section illustrates the modeling of crack evolution on multi-patch shells with the constraints from Sec. 5. Note that the gradients of ϕ are now defined in the reference configuration and the constraint from Eq. (76) is considered. The following material parameters are used throughout this section (see Eqs. (16)–(17))

$$K = \frac{E\nu}{(1+\nu)(1-2\nu)}, \quad G = \frac{E}{2(1+\nu)}, \quad c = 0.1 E_0 L_0, \quad (97)$$

with 2D Young's modulus E and Poisson's ratio ν . All quantities in this section are dimensionless by the introduction of a reference length L_0 , time T_0 and density ρ_0 . From this, the reference stiffness $E_0 := \rho_0 L_0^2 T_0^{-2}$ with units [N/m] follows (Paul et al., 2019). The color coding for the fracture field ranges from the fully fractured state ($\phi = 0$, red color) to the undamaged state ($\phi = 1$, blue color), see Fig. 1b. The lines of reduced continuity are again referred to as C^0 -lines.

6.3.1 Verification of the constraint on the fracture field

This section is intended to verify the constraint from Eq. (76) in a two-dimensional setup without mechanical loading. The flat sheet shown in Fig. 18a is considered. The length scale parameter is $\ell_0 = 0.008 L_0$ and the fracture toughness is $\mathcal{G}_c = 0.0005 E_0 L_0$. The used LR mesh is shown in Fig. 18b. The three C^0 -lines are inserted by knot insertion. The crack in Fig. 18a is computed by solving the phase field equation and manually imposing values for the history field (Borden et al., 2012), see Eq. (35). Fig. 19a illustrates the absolute value of the constraint g_∇ along

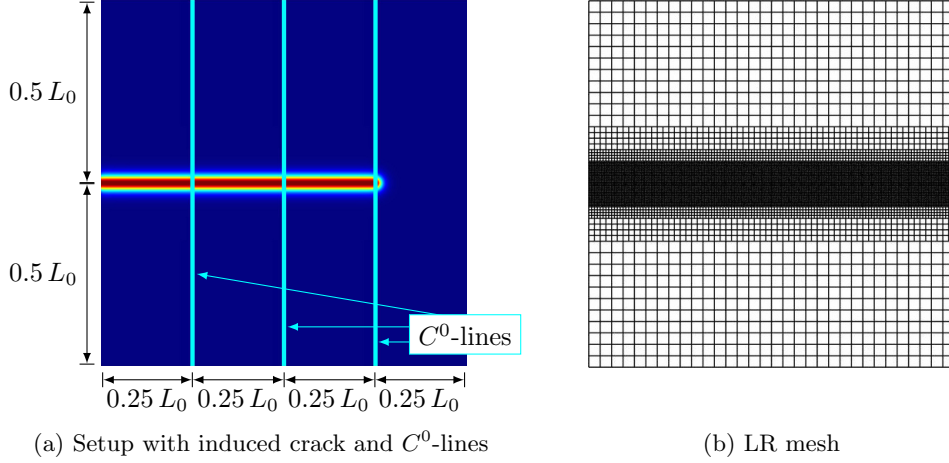


Figure 18: Verification of the constraint on the fracture field. (a) Setup showing the induced initial crack and three C^0 -lines treated with the Lagrange multiplier method using linear interpolation. (b) LR mesh used for all computations.

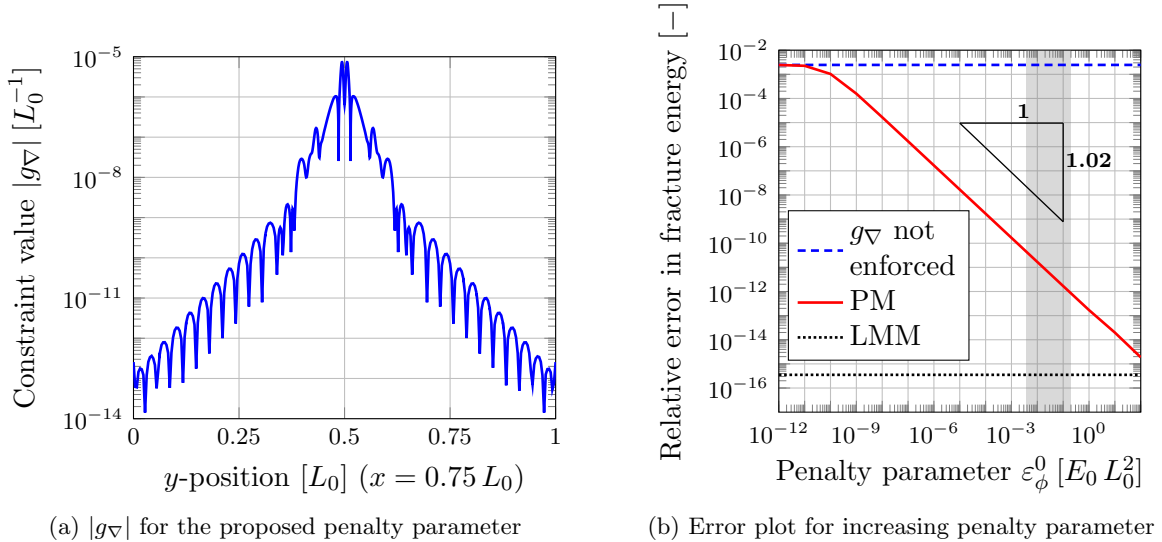


Figure 19: Verification of the constraint on the fracture field. (a) The absolute value of the phase field constraint along the third C^0 -line (at $x = 0.75 L_0$) for the penalty parameter ε_ϕ according to Eq. (87). (b) Relative error in the fracture energy for different enforcement techniques and increasing penalty parameter. The gray marked area shows the range of the proposed penalty parameter according to Eq. (87).

the third C^0 -line (at $x = 0.75 L_0$) over the y -position using the penalty method. Maximum values are obtained at the center where the crack is located. The Lagrange multiplier method with constant or linear interpolation leads to values of order 10^{-12} for $|g_\nabla|$. Fig. 19b shows the relative error in the fracture energy for an increasing penalty parameter. The fracture energy of the sheet without manually inserted C^0 -lines is taken as a reference solution. As the penalty parameter increases, the relative error decreases approximately linear until it is close to machine precision. Divergence is encountered beyond $\varepsilon_\phi^0 = 10^3 E_0 L_0$ due to ill-conditioning. The gray marked area reflects the range of the proposed penalty parameter from Eq. (87). Its largest values are obtained at regions of the highest resolved mesh. It ensures sufficiently accurate results while providing good convergence of the Newton-Raphson scheme. Machine precision is directly reached when the Lagrange multiplier method is used. The blue dashed line marks the error when no constraints are enforced. In this case, the insufficient discretization yields comparatively high errors that can have a huge influence on the solution as loads are applied.

6.3.2 Fracturing sphere

This section investigates crack evolution on a spherical shell with radius L_0 . Two initial cracks with perpendicular orientation are placed on two opposite sides of the sphere, as shown in Fig. 20a. The sphere is subjected to the internal pressure p .¹¹ Fig. 20a also shows the positions of the patch interfaces. The unstructured spline discretization with $r = 2$ (see Fig. 14) is used as a reference solution. For all computations in this section, $m = 32$ (see Fig. 14) is used for the six-patch discretization. In this section, a constant penalty parameter ε_ϕ , which does not depend on mesh or time step sizes, is used. The material parameters are listed in Table 4. The parameter ℓ_0 is chosen in a way, such that the interface is properly resolved for both kind of discretizations.

Table 4: Fracturing sphere: Material parameters and imposed internal pressure.

$E [E_0]$	$\nu [-]$	$\mathcal{G}_c [E_0 L_0]$	$\ell_0 [L_0]$	$T [L_0]$	$p [E_0 L_0^{-1}]$
10	0.3	0.0005	0.05	0.0125	0.1

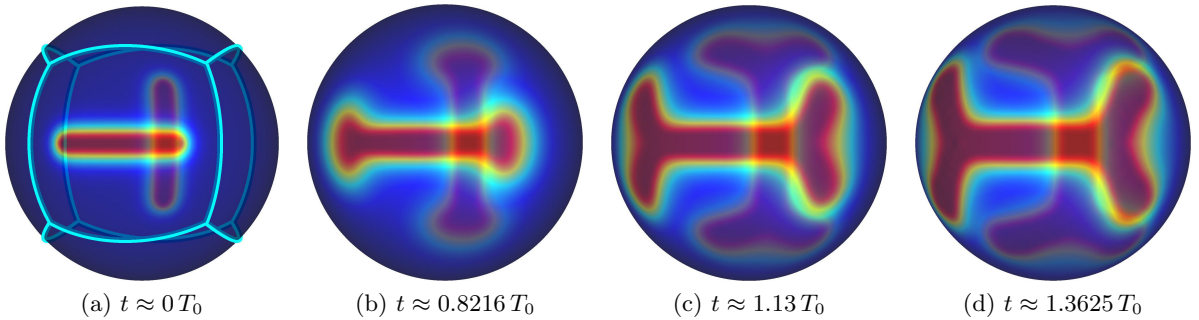


Figure 20: Fracturing sphere: Crack evolution using the six-patch discretization and the Lagrange multipliers method with linear interpolation for both constraints. The sphere is visualized transparently.

The evolution of the crack is illustrated in Fig. 20. At first, the cracks propagate along their initial direction, but then start branching. In the process, they cross several patch interfaces.

¹¹Note that here, the pressure is not depending on the phase field as in Paul et al. (2019).

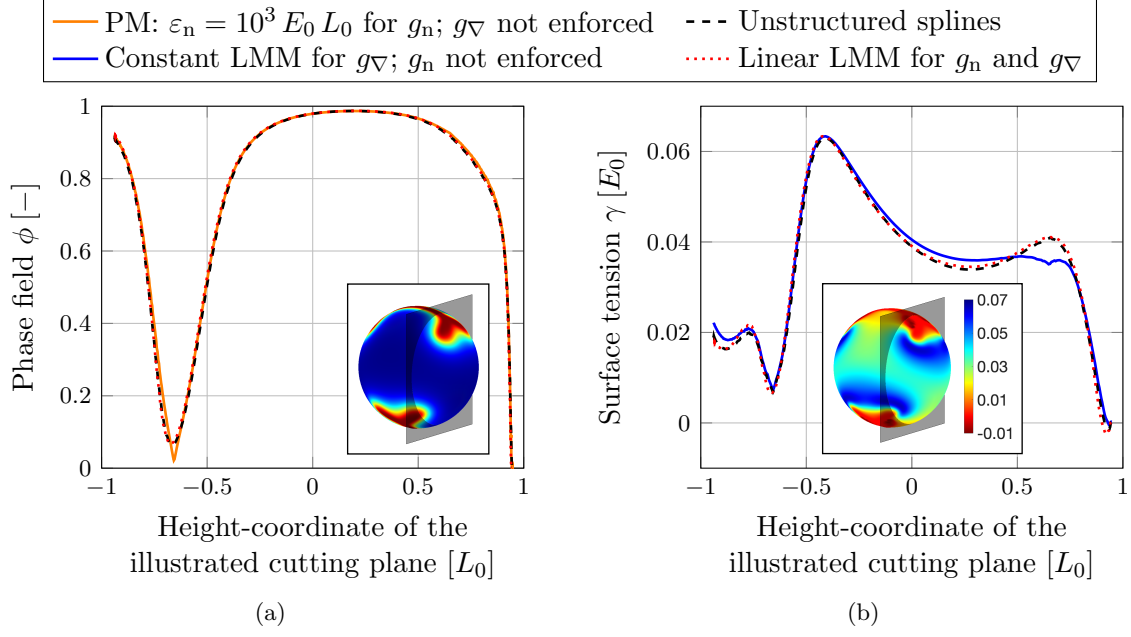


Figure 21: Fracturing sphere: (a) Phase field value and (b) surface tension along the height-coordinate of the shown cutting plane. Neglecting one constraint leads to significant offsets in the corresponding curves.

Fig. 21 shows the phase field value and surface tension over the height-coordinate of the illustrated cutting planes. The curves for the Lagrange multiplier method with linear interpolation and the unconstrained reference solution based on the unstructured spline discretization coincide very well. The solid line in both figures shows the profile if one of the constraints is neglected. If the phase field constraint is neglected, a kink will appear in ϕ at position $\approx -0.65 L_0$, as the figure shows. These kinks are avoided if the constraint is fulfilled. Further inaccuracies for γ can be observed at $\approx \{-0.93, -0.65, 0.2, 0.65, 0.94\} L_0$. The effect on the phase field and surface tension when either g_∇ or g_n are ignored, are illustrated in Figs. 22–23. If the phase field is

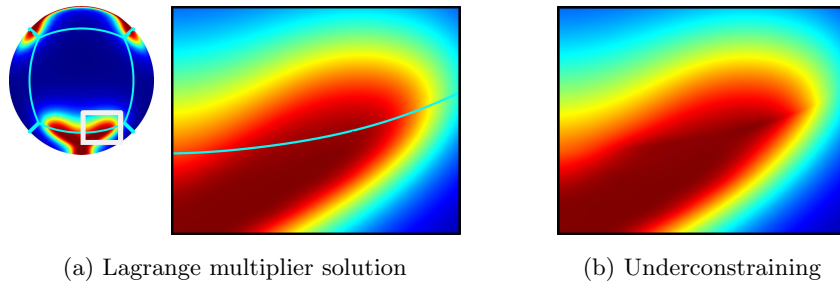


Figure 22: Fracturing sphere: (a) Phase field at $t \approx 1.13 T_0$ for the Lagrange multiplier method with linear interpolation. The enlargement is shown next to it. (b) The effect of a too small penalty parameter ($\varepsilon_\phi = 0$) on the phase field (the patch line is not plotted in order to show this better).

underconstrained, it is discontinuous at the interface, see Fig. 22b. Finally, the effect of an insufficient enforcement of the G^1 -continuity constraint is shown in Fig. 23. Major peaks in the surface tension appear at the patch interfaces, see Fig. 23a. Figs. 23b–23d show the surface tension for different enforcement techniques in comparison to a fully C^1 -continuous discretization

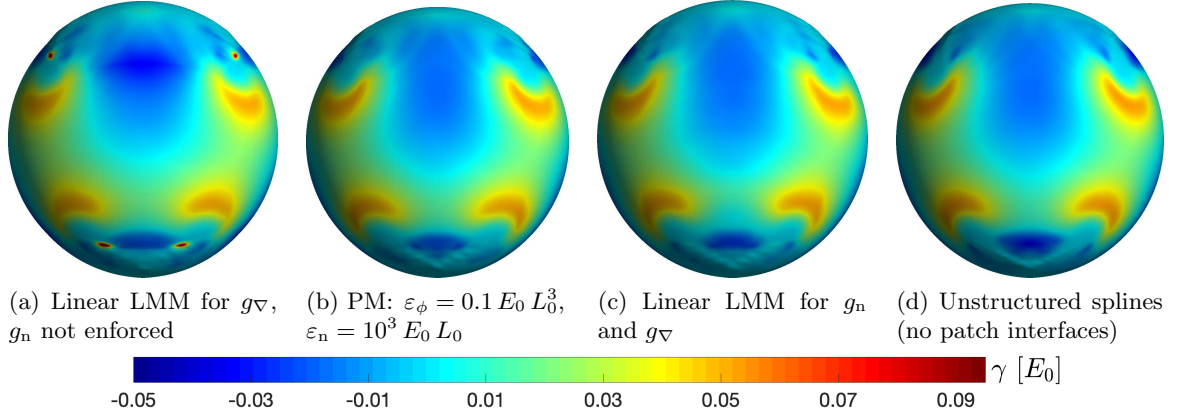


Figure 23: Fracturing sphere: Surface tension at $t \approx 1.3263 T_0$ for different patch constraint enforcement techniques.

at $t \approx 1.3263 T_0$.¹² Again, the results from the different discretization techniques show excellent agreement.

6.3.3 Crack propagation across kinks

This section focuses on the general constraints for non-smooth patch connections. The initial setup with an existing initial crack is shown in Fig. 24–25a. The mesh is locally refined a priori based on the expected crack path, see Fig. 25b. The refinement depth is $d = 3$ (Paul et al., 2019). The material parameters are listed in Table 5. A displacement is applied as shown

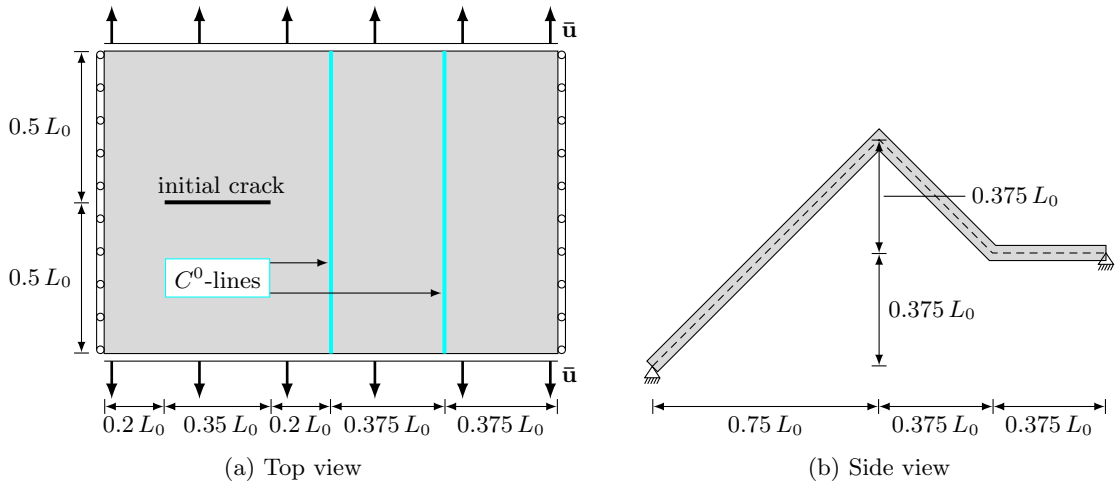


Figure 24: Crack propagation across kinks: Geometry with initial crack. The two C^0 -lines are marked by bold cyan-colored lines.

in Fig. 24a. At each time step, the displacement increment $\Delta \bar{u} = \bar{v} \Delta t$ is imposed to obtain a constant loading velocity \bar{v} . The crack evolution is illustrated in Fig. 26 for four different time steps. The crack starts propagating into both directions. While one end reaches the end of the sheet on the left, the right end propagates across the kink. Crack branching occurs shortly before the crack reaches the second kink. A very similar fracture pattern is observed when

¹²Note that the time steps for the shown snapshots slightly differ due to the adaptive time stepping scheme.

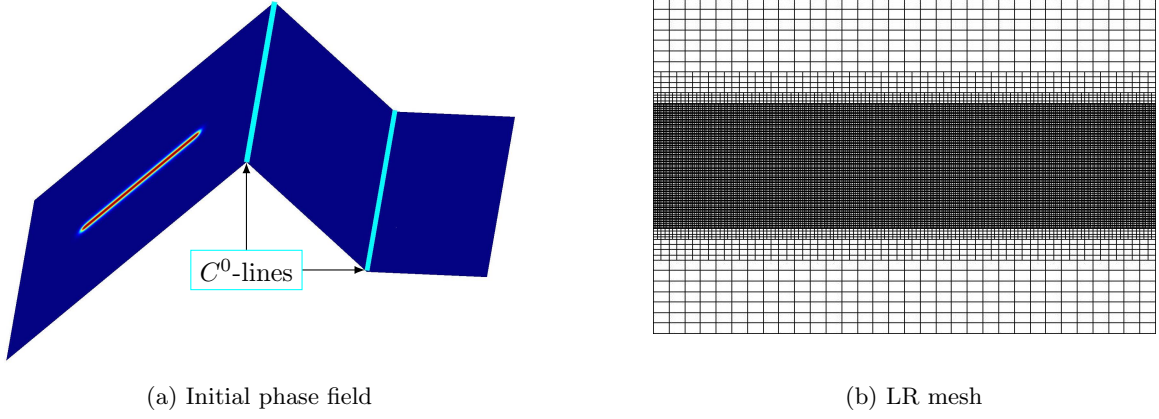


Figure 25: Crack propagation across kinks: (a) Initial phase field and (b) LR mesh that is locally refined a priori based on the expected crack path.

Table 5: Crack propagation across kinks: Material parameters and loading velocity \bar{v} .

$E [E_0]$	$\nu [-]$	$\mathcal{G}_c [E_0 L_0]$	$\ell_0 [L_0]$	$T [L_0]$	$\bar{v} [L_0 T_0^{-1}]$
100	0.3	0.0005	0.008	0.0125	0.004

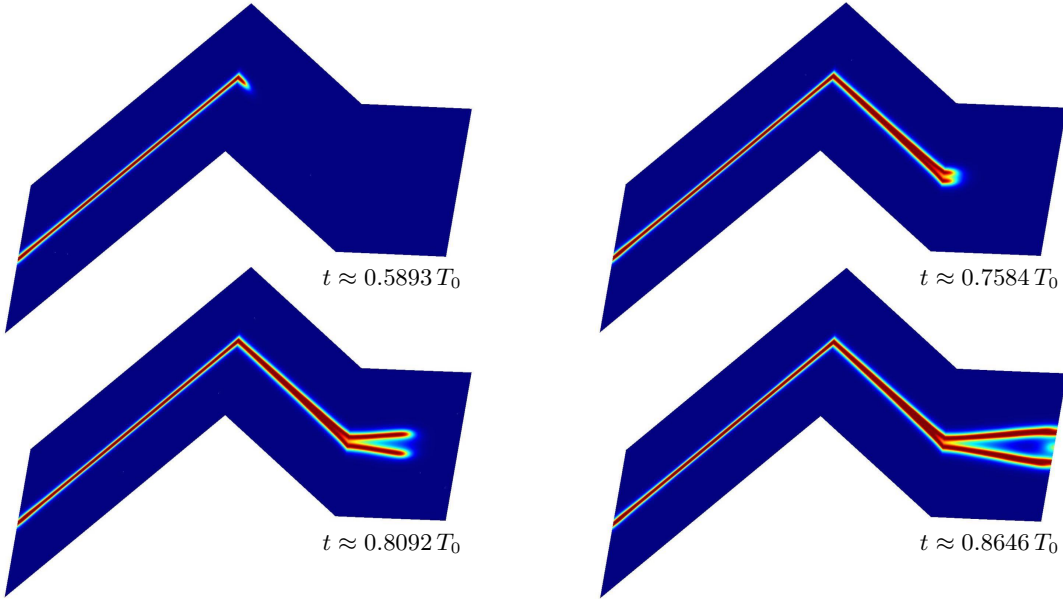


Figure 26: Crack propagation across kinks: Crack evolution where both constraints are fulfilled via the Lagrange multiplier method with constant interpolation.

the two surface kinks are smoothed and a fully C^1 -continuous parametrization is used. If the phase field constraint is neglected, the phase field will smear at the two kinks and will slightly evolve along them, similar as in Fig. 22b. So it can be concluded that crack evolution including branching works well in the proposed framework.

7 Conclusion

This work proposes continuity constraints for coupled fourth-order deformation and phase field models discretized by isogeometric multi-patch shells. The higher continuity that stems from IGA is not automatically preserved at the patch interfaces. The G^1 - and C^1 -continuity is recovered by enforcing patch constraints with a penalty or Lagrange multiplier approach. The interfaces between the patches are assumed to be conforming with respect to the discretization, but allow for non-smooth connections, for example to model kinks in the geometry. The constraints are fully formulated in the convective coordinate system that arises from the surface description and are thus, applicable to the majority of shell formulations.

In Sec. 6, both, the pure shell framework and the coupled one of phase field models on deforming surfaces, are investigated. The first is used within a quasi-static framework to compare the solutions using patch constraints to analytical solutions. The enforcement techniques perform well in terms of convergence rates and absolute errors. The coupled framework includes phase transitions, which are based on the Cahn-Hilliard equation, on deforming surfaces, and brittle fracture of thin shells. The latter is based on a phase field approach in which the transition between undamaged and fully fractured material is smeared. The results for the phase separation highlight the importance of the C^1 -continuity constraint. If the constraint is neglected, the concentration field will cluster along the patch interfaces and wrong phase distribution occurs. Comparison with fully C^1 -continuous discretizations demonstrate correct functioning of the proposed constraints and enforcement techniques. Similar conclusions are drawn for brittle fracture. The example studying crack propagation across kinks shows the capability of our formulation to handle non-smooth patch connections. Local refinement based on LR NURBS is used for this example. Inserting appropriate meshlines, they can also be employed to make non-conforming meshes conforming. An insufficient inter-patch continuity can lead to peaks in the stresses or in a smearing of the fracture field at the patch interfaces. The investigations on the penalty parameter demonstrate the suitable choice of the proposed problem-independent penalty parameter for the constraint on the fracture field.

Possible extensions to this work include the coupling of the G^1 - and C^1 -continuity constraints with each other. For example in the fracture framework, the G^1 -constraint may be neglected in fully fractured regions. The enforcement techniques may also be extended to handle non-conforming meshes, e.g. by a modified penalty or mortar method (see Sec. 1). An extension to the coupling of trimmed or unstructured splines may be of interest, especially for geometries that are created by CAD software. The present work focuses on solid materials. Modeling phase separation and fracture of fluidic shells, such as lipid bilayers, which can also be described by the present shell formulation (Sauer et al., 2017), is another extension.

Acknowledgments

The authors acknowledge funding by the Deutsche Forschungsgemeinschaft (DFG, German Research Foundation) projects GSC 111 (Graduate School AICES) and 33849990/GRK2379 (IRTG Modern Inverse Problems). Simulations in Sec. 6.3 were performed with computing resources granted by RWTH Aachen University under project rwth0433. The authors also thank Deepesh Toshniwal for providing the unstructured spline discretization used in Sec. 6.

Appendix

A Auxiliary variations

This section states and derives several variations that occur in Sec. 5. The variation of Eq. (59) requires the variations of the terms $\cos \alpha$ and $\sin \alpha$. They follow from Eqs. (52) and (54) as

$$\delta(\cos \alpha) = \delta(\mathbf{n} \cdot \tilde{\mathbf{n}}) = \delta \mathbf{n} \cdot \tilde{\mathbf{n}} + \mathbf{n} \cdot \delta \tilde{\mathbf{n}}, \quad (98)$$

and

$$\begin{aligned} \delta(\sin \alpha) &= \delta\left((\mathbf{n} \times \tilde{\mathbf{n}}) \cdot \boldsymbol{\tau}\right) = (\delta \mathbf{n} \times \tilde{\mathbf{n}}) \cdot \boldsymbol{\tau} + (\mathbf{n} \times \delta \tilde{\mathbf{n}}) \cdot \boldsymbol{\tau} + (\mathbf{n} \times \tilde{\mathbf{n}}) \cdot \delta \boldsymbol{\tau} \\ &= -(\delta \mathbf{n} \times \tilde{\mathbf{n}}) \cdot \tilde{\boldsymbol{\tau}} - (\delta \tilde{\mathbf{n}} \times \mathbf{n}) \cdot \boldsymbol{\tau} + (\mathbf{n} \times \tilde{\mathbf{n}}) \cdot \delta \boldsymbol{\tau} \\ &= -(\tilde{\mathbf{n}} \times \tilde{\boldsymbol{\tau}}) \cdot \delta \mathbf{n} - (\mathbf{n} \times \boldsymbol{\tau}) \cdot \delta \tilde{\mathbf{n}} + (\mathbf{n} \times \tilde{\mathbf{n}}) \cdot \delta \boldsymbol{\tau} \\ &= \tilde{\boldsymbol{\nu}} \cdot \delta \mathbf{n} + \boldsymbol{\nu} \cdot \delta \tilde{\mathbf{n}} + (\mathbf{n} \times \tilde{\mathbf{n}}) \cdot \delta \boldsymbol{\tau}. \end{aligned} \quad (99)$$

Using Eqs. (98) and (99), the following relations can be derived

$$\begin{aligned} \delta(\cos(\alpha - \alpha_0)) &= \delta(c_0 \cos(\alpha) + s_0 \sin(\alpha)) \\ &= c_0(\delta \mathbf{n} \cdot \tilde{\mathbf{n}} + \mathbf{n} \cdot \delta \tilde{\mathbf{n}}) + s_0(\delta \boldsymbol{\tau} \cdot (\mathbf{n} \times \tilde{\mathbf{n}}) + \delta \mathbf{n} \cdot \tilde{\boldsymbol{\nu}} + \delta \tilde{\mathbf{n}} \cdot \boldsymbol{\nu}), \end{aligned} \quad (100)$$

and

$$\begin{aligned} \delta(\sin(\alpha - \alpha_0)) &= \delta(c_0 \sin(\alpha) - s_0 \cos(\alpha)) \\ &= c_0(\delta \boldsymbol{\tau} \cdot (\mathbf{n} \times \tilde{\mathbf{n}}) + \delta \mathbf{n} \cdot \tilde{\boldsymbol{\nu}} + \delta \tilde{\mathbf{n}} \cdot \boldsymbol{\nu}) - s_0(\delta \mathbf{n} \cdot \tilde{\mathbf{n}} + \mathbf{n} \cdot \delta \tilde{\mathbf{n}}), \end{aligned} \quad (101)$$

which are required in Sec. 5.1.3.

Further variations that are required in Sec. 5.1 are (Sauer, 2014; Duong et al., 2017)

$$\delta \mathbf{n} = -(\mathbf{a}^\alpha \otimes \mathbf{n}) \delta \mathbf{a}_\alpha, \quad \delta \tilde{\mathbf{n}} = -(\tilde{\mathbf{a}}^\alpha \otimes \tilde{\mathbf{n}}) \delta \tilde{\mathbf{a}}_\alpha, \quad \delta \boldsymbol{\tau} = \mathbf{M}^s \delta \hat{\mathbf{a}}_s, \quad (102)$$

with the variation of $\hat{\mathbf{a}}_s$ from Eq. (48) and

$$\mathbf{M}^s := \frac{1}{\|\hat{\mathbf{a}}_s\|} (\mathbf{1} - \boldsymbol{\tau} \otimes \boldsymbol{\tau}). \quad (103)$$

B Linearization of C^1 -continuity constraints

In this section, the linearization of the force vectors stemming from the C^1 -continuity constraint in Sec. 5.2 is derived. Note that the linearization of the force vectors for the G^1 -continuity constraint in Sec. 5.1 can be found in Duong et al. (2017). Some auxiliary linearized quantities, such as the linearized constraint g_∇ from Eq. (77), are derived in Appendix B.1. These will then be used to obtain the linearization of the penalty method in Appendix B.2 and the linearization of the Lagrange multiplier method in Appendix B.3. The linearization is reported for the most general expression of the force vectors. The linearization for the fracture model will significantly simplify, since the corresponding force vectors do not depend on \mathbf{x} or $\tilde{\mathbf{x}}$, but only on \mathbf{X} and $\tilde{\mathbf{X}}$. Thus, the linearization with respect to \mathbf{x} and $\tilde{\mathbf{x}}$ vanishes for the brittle fracture model. Additionally, the simplification $\tilde{\boldsymbol{\nu}} = -\boldsymbol{\nu}$ can be inserted for smooth patch connections. Here, the G^1 -continuity constraint is not depending on any of the phase fields, so that the corresponding force vectors do not require any linearization with respect to ϕ or $\tilde{\phi}$.

B.1 Linearization of auxiliary quantities

For the linearization of the constraint in Eq. (77), further linearizations of surface measures are required, for example (Sauer and Duong, 2017; Zimmermann et al., 2019)

$$\begin{aligned}\Delta_{\mathbf{x}} \mathbf{a}^\alpha &= (a^{\alpha\beta} \mathbf{n} \otimes \mathbf{n} - \mathbf{a}^\beta \otimes \mathbf{a}^\alpha) \mathbf{N}_{,\beta} \Delta \mathbf{x}_e, \\ \Delta_{\mathbf{x}} \boldsymbol{\nu} &= -(\boldsymbol{\tau} \otimes \boldsymbol{\nu}) \Delta_{\mathbf{x}} \boldsymbol{\tau} - (\mathbf{n} \otimes \boldsymbol{\nu}) \Delta_{\mathbf{x}} \mathbf{n},\end{aligned}\tag{104}$$

with

$$\begin{aligned}\Delta_{\mathbf{x}} \mathbf{n} &= -\mathbf{a}^\alpha (\mathbf{n} \cdot \Delta_{\mathbf{x}} \mathbf{a}_\alpha) = -(\mathbf{a}^\alpha \otimes \mathbf{n}) \Delta_{\mathbf{x}} \mathbf{a}_\alpha, \\ \Delta_{\mathbf{x}} \boldsymbol{\tau} &= \mathbf{M}^s \Delta_{\mathbf{x}} \hat{\mathbf{a}}_s,\end{aligned}\tag{105}$$

see Eqs. (102)–(103). For simplicity, the following notation is introduced for the quantities in Eq. (104)

$$\Delta_{\mathbf{x}} \mathbf{a}^\alpha := \mathbf{A}^\alpha \Delta \mathbf{x}_e, \quad \text{and} \quad \Delta_{\mathbf{x}} \boldsymbol{\nu} := \mathbf{V} \Delta \mathbf{x}_e,\tag{106}$$

with the definitions

$$\begin{aligned}\mathbf{A}^\alpha &:= (a^{\alpha\beta} \mathbf{n} \otimes \mathbf{n} - \mathbf{a}^\beta \otimes \mathbf{a}^\alpha) \mathbf{N}_{,\beta}, \\ \mathbf{V} &:= -(\boldsymbol{\tau} \otimes \boldsymbol{\nu}) \mathbf{M}^s \hat{\mathbf{N}}_{,s} + (\mathbf{n} \otimes \boldsymbol{\nu}) (\mathbf{a}^\alpha \otimes \mathbf{n}) \mathbf{N}_{,\alpha}.\end{aligned}\tag{107}$$

Note that the quantities in Eq. (107) have dimension $3 \times 3 n_e$, where n_e denotes the number of control points associated with the element Ω^e . The quantity $\Delta \mathbf{x}_e$ has dimension $3 n_e \times 1$. The corresponding auxiliary variables $\tilde{\mathbf{A}}^\alpha$ and $\tilde{\mathbf{V}}$ follow in analogy to Eq. (107), i.e.

$$\begin{aligned}\tilde{\mathbf{A}}^\alpha &:= (\tilde{a}^{\alpha\beta} \tilde{\mathbf{n}} \otimes \tilde{\mathbf{n}} - \tilde{\mathbf{a}}^\beta \otimes \tilde{\mathbf{a}}^\alpha) \tilde{\mathbf{N}}_{,\beta}, \\ \tilde{\mathbf{V}} &:= -(\tilde{\boldsymbol{\tau}} \otimes \tilde{\boldsymbol{\nu}}) \mathbf{M}^{\tilde{s}} \tilde{\mathbf{N}}_{,\tilde{s}} + (\tilde{\mathbf{n}} \otimes \tilde{\boldsymbol{\nu}}) (\tilde{\mathbf{a}}^\alpha \otimes \tilde{\mathbf{n}}) \tilde{\mathbf{N}}_{,\alpha},\end{aligned}\tag{108}$$

so that $\Delta_{\tilde{\mathbf{x}}} \tilde{\mathbf{a}}^\alpha := \tilde{\mathbf{A}}^\alpha \Delta \tilde{\mathbf{x}}_e$ and $\Delta_{\tilde{\mathbf{x}}} \tilde{\boldsymbol{\nu}} := \tilde{\mathbf{V}} \Delta \tilde{\mathbf{x}}_e$. Note that the simplifications $\tilde{\boldsymbol{\tau}} = -\boldsymbol{\tau}$ and $\tilde{s} = -s$ can be inserted for conforming meshes, see Fig. 3.

The individual linearizations of the Lagrange multiplier λ (cf. Sec. 5.2.3) are

$$\Delta_\phi \lambda = 0, \quad \Delta_{\tilde{\phi}} \lambda = 0, \quad \Delta_{\mathbf{x}} \lambda = 0, \quad \Delta_{\tilde{\mathbf{x}}} \lambda = 0, \quad \Delta_\lambda \lambda = \mathbf{N}_\lambda \Delta \lambda_e,\tag{109}$$

with shape function array \mathbf{N}_λ of dimension $1 \times n_\lambda$ and corresponding linearized nodal values $\Delta \lambda_e$ of size $n_\lambda \times 1$, see Eq. (91). The variable n_λ depends on the order of approximation of the Lagrange multiplier, see Fig. 2.

Based on Eqs. (106)–(109), the individual linearizations of the C^1 -continuity constraint in Eq. (77) are given by

$$\begin{aligned}\Delta_\phi g_\nabla &= (\mathbf{a}^\alpha \cdot \boldsymbol{\nu}) \bar{\mathbf{N}}_{,\alpha} \Delta \phi_e, \\ \Delta_{\tilde{\phi}} g_\nabla &= (\tilde{\mathbf{a}}^\alpha \cdot \tilde{\boldsymbol{\nu}}) \tilde{\bar{\mathbf{N}}}_{,\alpha} \Delta \tilde{\phi}_e, \\ \Delta_{\mathbf{x}} g_\nabla &= \phi_{,\alpha} (\boldsymbol{\nu} \cdot \mathbf{A}^\alpha + \mathbf{a}^\alpha \cdot \mathbf{V}) \Delta \mathbf{x}_e, \\ \Delta_{\tilde{\mathbf{x}}} g_\nabla &= \tilde{\phi}_{,\alpha} (\tilde{\boldsymbol{\nu}} \cdot \tilde{\mathbf{A}}^\alpha + \tilde{\mathbf{a}}^\alpha \cdot \tilde{\mathbf{V}}) \Delta \tilde{\mathbf{x}}_e, \\ \Delta_\lambda g_\nabla &= 0.\end{aligned}\tag{110}$$

Additionally, the linearization of the terms $(\mathbf{a}^\alpha \cdot \boldsymbol{\nu})$ and $(\tilde{\mathbf{a}}^\alpha \cdot \tilde{\boldsymbol{\nu}})$ will be required, since both of them occur in the force vectors in Eqs. (85) and (93). The linearizations are given by

$$\begin{aligned}\Delta_\phi (\mathbf{a}^\alpha \cdot \boldsymbol{\nu}) &= 0, & \Delta_{\tilde{\phi}} (\mathbf{a}^\alpha \cdot \boldsymbol{\nu}) &= 0, & \Delta_{\mathbf{x}} (\mathbf{a}^\alpha \cdot \boldsymbol{\nu}) &= (\boldsymbol{\nu} \cdot \mathbf{A}^\alpha + \mathbf{a}^\alpha \cdot \mathbf{V}) \Delta \mathbf{x}_e, \\ \Delta_{\tilde{\mathbf{x}}} (\mathbf{a}^\alpha \cdot \boldsymbol{\nu}) &= 0, & \Delta_\lambda (\mathbf{a}^\alpha \cdot \boldsymbol{\nu}) &= 0,\end{aligned}\tag{111}$$

and

$$\begin{aligned}\Delta_\phi(\tilde{\mathbf{a}}^\alpha \cdot \boldsymbol{\nu}) &= 0, & \Delta_{\tilde{\phi}}(\tilde{\mathbf{a}}^\alpha \cdot \boldsymbol{\nu}) &= 0, & \Delta_{\mathbf{x}}(\tilde{\mathbf{a}}^\alpha \cdot \boldsymbol{\nu}) &= 0, \\ \Delta_{\tilde{\mathbf{x}}}(\tilde{\mathbf{a}}^\alpha \cdot \boldsymbol{\nu}) &= (\tilde{\boldsymbol{\nu}} \cdot \tilde{\mathbf{A}}^\alpha + \tilde{\mathbf{a}}^\alpha \cdot \tilde{\mathbf{V}}) \Delta \tilde{\mathbf{x}}_e, & \Delta_\lambda(\tilde{\mathbf{a}}^\alpha \cdot \boldsymbol{\nu}) &= 0.\end{aligned}\tag{112}$$

In the subsequent sections, the linearizations of the force vectors from the penalty and Lagrange multiplier method are reported.

B.2 Penalty method

This section shows the linearization of the force vectors \mathbf{f}_ϕ^e and $\mathbf{f}_{\tilde{\phi}}^e$ given in Eq. (85). Their contributions follow from

$$\Delta_\bullet \mathbf{f}_\phi^e = \int_{\Gamma^e} \varepsilon_\phi \bar{\mathbf{N}}_{,\alpha}^T \Delta_\bullet (g_\nabla(\mathbf{a}^\alpha \cdot \boldsymbol{\nu})) \, dS, \quad \text{and} \quad \Delta_\bullet \mathbf{f}_{\tilde{\phi}}^e = \int_{\Gamma^e} \varepsilon_\phi \tilde{\bar{\mathbf{N}}}_{,\alpha}^T \Delta_\bullet (g_\nabla(\tilde{\mathbf{a}}^\alpha \cdot \tilde{\boldsymbol{\nu}})) \, dS.\tag{113}$$

These are given by

$$\begin{aligned}\Delta_\phi \mathbf{f}_\phi^e &= \int_{\Gamma^e} \varepsilon_\phi \bar{\mathbf{N}}_{,\alpha}^T (\mathbf{a}^\alpha \cdot \boldsymbol{\nu}) (\mathbf{a}^\beta \cdot \boldsymbol{\nu}) \bar{\mathbf{N}}_{,\beta} \, dS \Delta \phi_e, \\ \Delta_{\tilde{\phi}} \mathbf{f}_{\tilde{\phi}}^e &= \int_{\Gamma^e} \varepsilon_\phi \bar{\mathbf{N}}_{,\alpha}^T (\mathbf{a}^\alpha \cdot \boldsymbol{\nu}) (\tilde{\mathbf{a}}^\beta \cdot \tilde{\boldsymbol{\nu}}) \tilde{\bar{\mathbf{N}}}_{,\beta} \, dS \Delta \tilde{\phi}_e, \\ \Delta_{\mathbf{x}} \mathbf{f}_\phi^e &= \int_{\Gamma^e} \varepsilon_\phi \bar{\mathbf{N}}_{,\alpha}^T \left[(\mathbf{a}^\alpha \cdot \boldsymbol{\nu}) \phi_{,\beta} (\boldsymbol{\nu} \cdot \mathbf{A}^\beta + \mathbf{a}^\beta \cdot \mathbf{V}) + g_\nabla(\boldsymbol{\nu} \cdot \mathbf{A}^\alpha + \mathbf{a}^\alpha \cdot \mathbf{V}) \right] \, dS \Delta \mathbf{x}_e, \\ \Delta_{\tilde{\mathbf{x}}} \mathbf{f}_{\tilde{\phi}}^e &= \int_{\Gamma^e} \varepsilon_\phi \bar{\mathbf{N}}_{,\alpha}^T (\mathbf{a}^\alpha \cdot \boldsymbol{\nu}) \tilde{\phi}_{,\beta} (\tilde{\boldsymbol{\nu}} \cdot \tilde{\mathbf{A}}^\beta + \tilde{\mathbf{a}}^\beta \cdot \tilde{\mathbf{V}}) \, dS \Delta \tilde{\mathbf{x}}_e,\end{aligned}\tag{114}$$

and

$$\begin{aligned}\Delta_\phi \mathbf{f}_\phi^e &= \int_{\Gamma^e} \varepsilon_\phi \tilde{\bar{\mathbf{N}}}_{,\alpha}^T (\tilde{\mathbf{a}}^\alpha \cdot \tilde{\boldsymbol{\nu}}) (\mathbf{a}^\beta \cdot \boldsymbol{\nu}) \bar{\mathbf{N}}_{,\beta} \, dS \Delta \phi_e, \\ \Delta_{\tilde{\phi}} \mathbf{f}_{\tilde{\phi}}^e &= \int_{\Gamma^e} \varepsilon_\phi \tilde{\bar{\mathbf{N}}}_{,\alpha}^T (\tilde{\mathbf{a}}^\alpha \cdot \tilde{\boldsymbol{\nu}}) (\tilde{\mathbf{a}}^\beta \cdot \tilde{\boldsymbol{\nu}}) \tilde{\bar{\mathbf{N}}}_{,\beta} \, dS \Delta \tilde{\phi}_e, \\ \Delta_{\mathbf{x}} \mathbf{f}_\phi^e &= \int_{\Gamma^e} \varepsilon_\phi \tilde{\bar{\mathbf{N}}}_{,\alpha}^T (\tilde{\mathbf{a}}^\alpha \cdot \tilde{\boldsymbol{\nu}}) \phi_{,\beta} (\boldsymbol{\nu} \cdot \mathbf{A}^\beta + \mathbf{a}^\beta \cdot \mathbf{V}) \, dS \Delta \mathbf{x}_e, \\ \Delta_{\tilde{\mathbf{x}}} \mathbf{f}_{\tilde{\phi}}^e &= \int_{\Gamma^e} \varepsilon_\phi \tilde{\bar{\mathbf{N}}}_{,\alpha}^T \left[(\tilde{\mathbf{a}}^\alpha \cdot \tilde{\boldsymbol{\nu}}) \tilde{\phi}_{,\beta} (\tilde{\boldsymbol{\nu}} \cdot \tilde{\mathbf{A}}^\beta + \tilde{\mathbf{a}}^\beta \cdot \tilde{\mathbf{V}}) + g_\nabla(\tilde{\boldsymbol{\nu}} \cdot \tilde{\mathbf{A}}^\alpha + \tilde{\mathbf{a}}^\alpha \cdot \tilde{\mathbf{V}}) \right] \, dS \Delta \tilde{\mathbf{x}}_e.\end{aligned}\tag{115}$$

Note that the linearizations in Eqs. (114.3)-(114.4) and Eqs. (115.3)-(115.4) vanish for the brittle fracture model. The element tangent matrix will have the following form

$$\begin{bmatrix} \boxed{\frac{\partial \mathbf{f}_\phi^e}{\partial \mathbf{x}_e}} & \boxed{\frac{\partial \mathbf{f}_\phi^e}{\partial \tilde{\mathbf{x}}_e}} & \frac{\partial \mathbf{f}_\phi^e}{\partial \phi_e} & \frac{\partial \mathbf{f}_\phi^e}{\partial \tilde{\phi}_e} \\ \boxed{\frac{\partial \mathbf{f}_{\tilde{\phi}}^e}{\partial \mathbf{x}_e}} & \boxed{\frac{\partial \mathbf{f}_{\tilde{\phi}}^e}{\partial \tilde{\mathbf{x}}_e}} & \frac{\partial \mathbf{f}_{\tilde{\phi}}^e}{\partial \phi_e} & \frac{\partial \mathbf{f}_{\tilde{\phi}}^e}{\partial \tilde{\phi}_e} \end{bmatrix}.\tag{116}$$

The dot-dashed framed entries vanish for the brittle fracture model.

B.3 Lagrange multiplier method

The contributions to the linearizations of the force vectors in Eq. (93) for the Lagrange multiplier method are computed from

$$\begin{aligned}\Delta_{\bullet} \bar{\mathbf{f}}_{\phi}^e &:= \int_{\Gamma^e} \bar{\mathbf{N}}_{,\alpha}^T \Delta_{\bullet} \left(\lambda (\mathbf{a}^{\alpha} \cdot \boldsymbol{\nu}) \right) dS, \\ \Delta_{\bullet} \bar{\mathbf{f}}_{\phi}^e &:= \int_{\Gamma^e} \tilde{\mathbf{N}}_{,\alpha}^T \Delta_{\bullet} \left(\lambda (\tilde{\mathbf{a}}^{\alpha} \cdot \tilde{\boldsymbol{\nu}}) \right) dS, \\ \Delta_{\bullet} \bar{\mathbf{f}}_{\lambda}^e &:= \int_{\Gamma^e} \mathbf{N}_{\lambda}^T \Delta_{\bullet} g_{\nabla} dS.\end{aligned}\tag{117}$$

They are given by

$$\begin{aligned}\Delta_{\phi} \bar{\mathbf{f}}_{\phi}^e &= \mathbf{0}, & \Delta_{\tilde{\phi}} \bar{\mathbf{f}}_{\phi}^e &= \mathbf{0}, & \Delta_{\mathbf{x}} \bar{\mathbf{f}}_{\phi}^e &= \int_{\Gamma^e} \bar{\mathbf{N}}_{,\alpha}^T \lambda (\boldsymbol{\nu} \cdot \mathbf{A}^{\alpha} + \mathbf{a}^{\alpha} \cdot \mathbf{V}) dS \Delta \mathbf{x}_e, \\ \Delta_{\tilde{\mathbf{x}}} \bar{\mathbf{f}}_{\phi}^e &= \mathbf{0}, & \Delta_{\lambda} \bar{\mathbf{f}}_{\phi}^e &= \int_{\Gamma^e} \bar{\mathbf{N}}_{,\alpha}^T (\mathbf{a}^{\alpha} \cdot \boldsymbol{\nu}) \mathbf{N}_{\lambda} dS \Delta \lambda_e,\end{aligned}\tag{118}$$

and

$$\begin{aligned}\Delta_{\phi} \bar{\mathbf{f}}_{\phi}^e &= \mathbf{0}, & \Delta_{\tilde{\phi}} \bar{\mathbf{f}}_{\phi}^e &= \mathbf{0}, & \Delta_{\mathbf{x}} \bar{\mathbf{f}}_{\phi}^e &= \mathbf{0}, \\ \Delta_{\tilde{\mathbf{x}}} \bar{\mathbf{f}}_{\phi}^e &= \int_{\Gamma^e} \tilde{\mathbf{N}}_{,\alpha}^T \lambda (\tilde{\boldsymbol{\nu}} \cdot \tilde{\mathbf{A}}^{\alpha} + \tilde{\mathbf{a}}^{\alpha} \cdot \tilde{\mathbf{V}}) dS \Delta \tilde{\mathbf{x}}_e, & \Delta_{\lambda} \bar{\mathbf{f}}_{\phi}^e &= \int_{\Gamma^e} \tilde{\mathbf{N}}_{,\alpha}^T (\tilde{\mathbf{a}}^{\alpha} \cdot \tilde{\boldsymbol{\nu}}) \mathbf{N}_{\lambda} dS \Delta \lambda_e,\end{aligned}\tag{119}$$

and

$$\begin{aligned}\Delta_{\phi} \bar{\mathbf{f}}_{\phi}^e &= \int_{\Gamma^e} \mathbf{N}_{\lambda}^T (\mathbf{a}^{\alpha} \cdot \boldsymbol{\nu}) \bar{\mathbf{N}}_{,\alpha} dS \Delta \phi_e, \\ \Delta_{\tilde{\phi}} \bar{\mathbf{f}}_{\phi}^e &= \int_{\Gamma^e} \mathbf{N}_{\lambda}^T (\tilde{\mathbf{a}}^{\alpha} \cdot \tilde{\boldsymbol{\nu}}) \tilde{\mathbf{N}}_{,\alpha} dS \Delta \tilde{\phi}_e, \\ \Delta_{\mathbf{x}} \bar{\mathbf{f}}_{\phi}^e &= \int_{\Gamma^e} \mathbf{N}_{\lambda}^T \phi_{,\alpha} (\boldsymbol{\nu} \cdot \mathbf{A}^{\alpha} + \mathbf{a}^{\alpha} \cdot \mathbf{V}) dS \Delta \mathbf{x}_e, \\ \Delta_{\tilde{\mathbf{x}}} \bar{\mathbf{f}}_{\phi}^e &= \int_{\Gamma^e} \mathbf{N}_{\lambda}^T \tilde{\phi}_{,\alpha} (\tilde{\boldsymbol{\nu}} \cdot \tilde{\mathbf{A}}^{\alpha} + \tilde{\mathbf{a}}^{\alpha} \cdot \tilde{\mathbf{V}}) dS \Delta \tilde{\mathbf{x}}_e, \\ \Delta_{\lambda} \bar{\mathbf{f}}_{\phi}^e &= \mathbf{0}.\end{aligned}\tag{120}$$

Note that the linearizations in Eqs. (118.3)-(118.4), Eqs. (119.3)-(119.4) and Eqs. (120.3)-(120.4) vanish for the brittle fracture model. The full element tangent matrix has the following form

$$\begin{bmatrix} \boxed{\frac{\partial \bar{\mathbf{f}}_{\phi}^e}{\partial \mathbf{x}_e}} & \mathbf{0} & \mathbf{0} & \mathbf{0} & \boxed{\frac{\partial \bar{\mathbf{f}}_{\phi}^e}{\partial \lambda_e}} \\ \mathbf{0} & \boxed{\frac{\partial \bar{\mathbf{f}}_{\phi}^e}{\partial \tilde{\mathbf{x}}_e}} & \mathbf{0} & \mathbf{0} & \boxed{\frac{\partial \bar{\mathbf{f}}_{\phi}^e}{\partial \lambda_e}} \\ \boxed{\frac{\partial \bar{\mathbf{f}}_{\lambda}^e}{\partial \mathbf{x}_e}} & \boxed{\frac{\partial \bar{\mathbf{f}}_{\lambda}^e}{\partial \tilde{\mathbf{x}}_e}} & \boxed{\frac{\partial \bar{\mathbf{f}}_{\lambda}^e}{\partial \phi_e}} & \boxed{\frac{\partial \bar{\mathbf{f}}_{\lambda}^e}{\partial \tilde{\phi}_e}} & \mathbf{0} \end{bmatrix}.\tag{121}$$

Note that one solid framed block is the transpose of the other solid framed block, while the dot-dashed framed entries vanish for the fracture model.

References

- Amor, H., Marigo, J.-J., and Maurini, C. (2009). Regularized formulation of the variational brittle fracture with unilateral contact: Numerical experiments. *Journal of the Mechanics and Physics of Solids*, **57**(8):1209–1229.
- Apostolatos, A., Bletzinger, K.-U., and Wehner, R. (2019). Weak imposition of constraints for structural membranes in transient geometrically nonlinear isogeometric analysis on multipatch surfaces. *Computer Methods in Applied Mechanics and Engineering*, **350**:938–994.
- Apostolatos, A., Schmidt, R., Wehner, R., and Bletzinger, K.-U. (2014). A Nitsche-type formulation and comparison of the most common domain decomposition methods in isogeometric analysis. *International Journal for Numerical Methods in Engineering*, **97**(7):473–504.
- Beirão da Veiga, L., Buffa, A., Cho, D., and Sangalli, G. (2011). IsoGeometric analysis using T-splines on two-patch geometries. *Computer Methods in Applied Mechanics and Engineering*, **200**(21):1787–1803.
- Belytschko, T., Stolarski, H., Liu, W. K., Carpenter, N., and Ong, J. S. (1985). Stress projection for membrane and shear locking in shell finite elements. *Computer Methods in Applied Mechanics and Engineering*, **51**(1):221–258.
- Borden, M. J., Hughes, T. J. R., Landis, C. M., Anvari, A., and Lee, I. J. (2016). A phase-field formulation for fracture in ductile materials: Finite deformation balance law derivation, plastic degradation, and stress triaxiality effects. *Computer Methods in Applied Mechanics and Engineering*, **312**:130–166.
- Borden, M. J., Hughes, T. J. R., Landis, C. M., and Verhoosel, C. V. (2014). A higher-order phase-field model for brittle fracture: Formulation and analysis within the isogeometric analysis framework. *Computer Methods in Applied Mechanics and Engineering*, **273**:100–118.
- Borden, M. J., Verhoosel, C. V., Scott, M. A., Hughes, T. J. R., and Landis, C. M. (2012). A phase-field description of dynamic brittle fracture. *Computer Methods in Applied Mechanics and Engineering*, **217–220**:77–95.
- Bouclier, R., Passieux, J.-C., and Salan, M. (2017). Development of a new, more regular, mortar method for the coupling of NURBS subdomains within a NURBS patch: Application to a non-intrusive local enrichment of NURBS patches. *Computer Methods in Applied Mechanics and Engineering*, **316**:123–150.
- Bourdin, B., Francfort, G., and Marigo, J.-J. (2000). Numerical experiments in revisited brittle fracture. *Journal of the Mechanics and Physics of Solids*, **48**(4):797–826.
- Cahn, J. W. (1961). On spinodal decomposition. *Acta Metallurgica*, **9**(9):795–801.
- Cahn, J. W. and Hilliard, J. E. (1958). Free Energy of a Nonuniform System. I. Interfacial Free Energy. *The Journal of Chemical Physics*, **28**(2):258–267.
- Chan, C. L., Anitescu, C., and Rabczuk, T. (2018). Isogeometric analysis with strong multipatch C1-coupling. *Computer Aided Geometric Design*, **62**:294–310.
- Chen, L. and de Borst, R. (2018). Locally Refined T-splines. *International Journal for Numerical Methods in Engineering*, **114**(6):637–659.
- Chung, J. and Hulbert, G. M. (1993). A time integration algorithm for structural dynamics with improved numerical dissipation: The generalized-alpha method. *Journal of Applied Mechanics*, **60**(2):371–375.

- Ciarlet, P. G. (1993). *Mathematical Elasticity: Three Dimensional Elasticity*. North-Holland.
- Collin, A., Sangalli, G., and Takacs, T. (2016). Analysis-suitable G1 multi-patch parametrizations for C1 isogeometric spaces. *Computer Aided Geometric Design*, **47**:93–113.
- Coox, L., Greco, F., Atak, O., Vandepitte, D., and Desmet, W. (2017). A robust patch coupling method for NURBS-based isogeometric analysis of non-conforming multipatch surfaces. *Computer Methods in Applied Mechanics and Engineering*, **316**:235–260.
- Dokken, T., Lyche, T., and Pettersen, K. F. (2013). Polynomial splines over locally refined box-partitions. *Computer Aided Geometric Design*, **30**(3):331–356.
- Dornisch, W., Vitucci, G., and Klinkel, S. (2015). The weak substitution method an application of the mortar method for patch coupling in NURBS-based isogeometric analysis. *International Journal for Numerical Methods in Engineering*, **103**(3):205–234.
- Du, X., Zhao, G., and Wang, W. (2015). Nitsche method for isogeometric analysis of Reissner-Mindlin plate with non-conforming multi-patches. *Computer Aided Geometric Design*, **35–36**:121–136.
- Duong, T. X., Roohbakhshan, F., and Sauer, R. A. (2017). A new rotation-free isogeometric thin shell formulation and a corresponding continuity constraint for patch boundaries. *Computer Methods in Applied Mechanics and Engineering*, **316**:43–83.
- Forsey, D. R. and Bartels, R. H. (1988). Hierarchical B-spline refinement. *SIGGRAPH Comput. Graph.*, **22**(4):205–212.
- Francfort, G. and Marigo, J.-J. (1998). Revisiting brittle fracture as an energy minimization problem. *Journal of the Mechanics and Physics of Solids*, **46**(8):1319–1342.
- Goyal, A. and Simeon, B. (2017). On penalty-free formulations for multipatch isogeometric Kirchhoff-Love shells. *Mathematics and Computers in Simulation*, **136**:78–103.
- Griffith, A. A. (1921). VI. The Phenomena of Rupture and Flow in Solids. *Philosophical Transactions of the Royal Society of London Series A*, **221**:163–198.
- Gu, J., Yu, T., Lich, L. V., Nguyen, T.-T., and Bui, T. Q. (2018). Adaptive multi-patch isogeometric analysis based on locally refined B-splines. *Computer Methods in Applied Mechanics and Engineering*, **339**:704–738.
- Guo, Y. and Ruess, M. (2015). Nitsches method for a coupling of isogeometric thin shells and blended shell structures. *Computer Methods in Applied Mechanics and Engineering*, **284**:881–905.
- Herrema, A. J., Johnson, E. L., Proserpio, D., Wu, M. C., Kiendl, J., and Hsu, M.-C. (2019). Penalty coupling of non-matching isogeometric Kirchhoff-Love shell patches with application to composite wind turbine blades. *Computer Methods in Applied Mechanics and Engineering*, **346**:810–840.
- Hirschler, T., Bouclier, R., Duval, A., Elguedj, T., and Morlier, J. (2019). The embedded isogeometric Kirchhoff-Love shell: From design to shape optimization of non-conforming stiffened multipatch structures. *Computer Methods in Applied Mechanics and Engineering*, **349**:774–797.
- Horger, T., Reali, A., Wohlmuth, B., and Wunderlich, L. (2019). A hybrid isogeometric approach on multi-patches with applications to Kirchhoff plates and eigenvalue problems. *Computer Methods in Applied Mechanics and Engineering*, **348**:396–408.

- Hu, Q., Chouly, F., Hu, P., Cheng, G., and Bordas, S. P. (2018). Skew-symmetric Nitsches formulation in isogeometric analysis: Dirichlet and symmetry conditions, patch coupling and frictionless contact. *Computer Methods in Applied Mechanics and Engineering*, **341**:188–220.
- Hughes, T. J. R., Cottrell, J. A., and Bazilevs, Y. (2005). Isogeometric analysis: CAD, finite elements, NURBS, exact geometry and mesh refinement. *Computer Methods in Applied Mechanics and Engineering*, **194**(39–41):4135–4195.
- Johannessen, K. A., Kvamsdal, T., and Dokken, T. (2014). Isogeometric analysis using LR B-splines. *Computer Methods in Applied Mechanics and Engineering*, **269**:471–514.
- Kiendl, J., Bazilevs, Y., Hsu, M.-C., Wchnner, R., and Bletzinger, K.-U. (2010). The bending strip method for isogeometric analysis of Kirchhoff-Love shell structures comprised of multiple patches. *Computer Methods in Applied Mechanics and Engineering*, **199**:2403–2416.
- Kiendl, J., Bletzinger, K.-U., Linhard, J., and Wchnner, R. (2009). Isogeometric shell analysis with Kirchhoff-Love elements. *Computer Methods in Applied Mechanics and Engineering*, **198**:3902–3914.
- Lei, Z., Gillot, F., and Jezequel, L. (2015). A C0/G1 multiple patches connection method in isogeometric analysis. *Applied Mathematical Modelling*, **39**(15):4405–4420.
- Macneal, R. H. and Harder, R. L. (1985). A proposed standard set of problems to test finite element accuracy. *Finite Elements in Analysis and Design*, **1**(1):3–20.
- Morley, L. and Morris, A. (1978). Conflict between finite elements and shell theory. Technical report, Royal Aircraft Establishment. Great Britain.
- Nguyen, V. P., Kerfriden, P., Brino, M., Bordas, S. P. A., and Bonisoli, E. (2014). Nitsche’s method for two and three dimensional NURBS patch coupling. *Computational Mechanics*, **53**(6):1163–1182.
- Paul, K., Zimmermann, C., Mandadapu, K. K., Hughes, T. J. R., Landis, C. M., and Sauer, R. A. (2019). An adaptive space-time phase field formulation for dynamic fracture of brittle shells based on LR NURBS. *Computational Mechanics (accepted)*, *arXiv:1906.10679*.
- Ruess, M., Schilling, D., Özcan, A. I., and Rank, E. (2014). Weak coupling for isogeometric analysis of non-matching and trimmed multi-patch geometries. *Computer Methods in Applied Mechanics and Engineering*, **269**:46–71.
- Sahu, A., Sauer, R. A., and Mandadapu, K. K. (2017). Irreversible thermodynamics of curved lipid membranes. *Physical Review E*, **96**:042409.
- Sauer, R. A. (2014). Stabilized finite element formulations for liquid membranes and their application to droplet contact. *International Journal for Numerical Methods in Fluids*, **75**(7):519–545.
- Sauer, R. A. (2018). On the computational modeling of lipid bilayers using thin-shell theory. In Steigmann, D. J., editor, *The Role of Mechanics in the Study of Lipid Bilayers*, pages 221–286. Springer International Publishing, Cham.
- Sauer, R. A. and Duong, T. X. (2017). On the theoretical foundations of thin solid and liquid shells. *Mathematics and Mechanics of Solids*, **22**(3):343–371.
- Sauer, R. A., Duong, T. X., Mandadapu, K. K., and Steigmann, D. J. (2017). A stabilized finite element formulation for liquid shells and its application to lipid bilayers. *Journal of Computational Physics*, **330**:436–466.

- Sauer, R. A., Ghaffari, R., and Gupta, A. (2019). The multiplicative deformation split for shells with application to growth, chemical swelling, thermoelasticity, viscoelasticity and elastoplasticity. *International Journal of Solids and Structures*, **174-175**:53–68.
- Schu, S., Dittmann, M., Wohlmuth, B., Klinkel, S., and Hesch, C. (2019). Multi-patch isogeometric analysis for Kirchhoff-Love shell elements. *Computer Methods in Applied Mechanics and Engineering*, **349**.
- Scott, M., Li, X., Sederberg, T., and Hughes, T. J. R. (2012). Local refinement of analysis-suitable T-splines. *Computer Methods in Applied Mechanics and Engineering*, **213**:206–222.
- Sederberg, T. W., Zheng, J., Bakenov, A., and Nasri, A. (2003). T-splines and T-NURCCs. *ACM Transactions on Graphics*, **22**(3):477–484.
- Sommerwerk, K., Woidt, M., Haupt, M. C., and Horst, P. (2017). ReissnerMindlin shell implementation and energy conserving isogeometric multi-patch coupling. *International Journal for Numerical Methods in Engineering*, **109**(7):982–1012.
- Toshniwal, D., Speleers, H., and Hughes, T. J. (2017). Smooth cubic spline spaces on unstructured quadrilateral meshes with particular emphasis on extraordinary points: Geometric design and isogeometric analysis considerations. *Computer Methods in Applied Mechanics and Engineering*, **327**:411–458.
- Zimmermann, C. and Sauer, R. A. (2017). Adaptive local surface refinement based on LR NURBS and its application to contact. *Computational Mechanics*, **60**:1011–1031.
- Zimmermann, C., Toshniwal, D., Landis, C. M., Hughes, T. J. R., Mandadapu, K. K., and Sauer, R. A. (2019). An isogeometric finite element formulation for phase transitions on deforming surfaces. *Computer Methods in Applied Mechanics and Engineering*, **351**:441–477.